research papers

We dedicate this paper to the memory of Dr A. McL. Mathieson, BSc (Aberdeen), PhD (Glasgow), DSc (Melbourne), Hon DSc (St Andrews), FAA, FRACI (1920–2011): a great mentor, colleague and friend, sadly missed. Sandy passed away peacefully in Melbourne on Tuesday 30 August 2011 at age 91 years. This was, in fact, the final day of the International Union of Crystallography's (IUCr) XXII Congress and General Assembly being held in Madrid; rather poignant given Sandy's staunch support of and significant contributions to the IUCr over many years. Sandy is widely recognized as the 'father of X-ray crystallography in Australia'.

Analysis and interpretation of the first monochromatic X-ray tomography data collected at the Australian Synchrotron Imaging and Medical beamline

Andrew W. Stevenson,[a]* Christopher J. Hall,[b] Sheridan C. Mayo,[a] Daniel Häusermann,[b] Anton Maksimenko,[b] Timur E. Gureyev,[a] Yakov I. Nesterets,[a] Stephen W. Wilkins[a,c] and Robert A. Lewis[d]

[a]CSIRO, Materials Science and Engineering, Private Bag 33, Clayton South, Victoria 3169, Australia, [b]Australian Synchrotron, 800 Blackburn Road, Clayton, Victoria 3168, Australia, [c]School of Physics, Monash University, Melbourne, Victoria 3800, Australia, and [d]Department of Medical Imaging and Radiation Sciences, Monash University, Melbourne, Victoria 3800, Australia. E-mail: andrew.stevenson@csiro.au

The first monochromatic X-ray tomography experiments conducted at the Imaging and Medical beamline of the Australian Synchrotron are reported. The sample was a phantom comprising nylon line, Al wire and finer Cu wire twisted together. Data sets were collected at four different X-ray energies. In order to quantitatively account for the experimental values obtained for the Hounsfield (or CT) number, it was necessary to consider various issues including the point-spread function for the X-ray imaging system and harmonic contamination of the X-ray beam. The analysis and interpretation of the data includes detailed considerations of the resolution and efficiency of the CCD detector, calculations of the X-ray spectrum prior to monochromatization, allowance for the response of the double-crystal Si monochromator used (via X-ray dynamical theory), as well as a thorough assessment of the role of X-ray phase-contrast effects. Computer simulations relating to the tomography experiments also provide valuable insights into these important issues. It was found that a significant discrepancy between theory and experiment for the Cu wire could be largely resolved in terms of the effect of the point-spread function. The findings of this study are important in respect of any attempts to extract quantitative information from X-ray tomography data, across a wide range of disciplines, including materials and life sciences.

1. Introduction

The first experiments conducted on the Imaging and Medical beamline (IMBL) at the Australian Synchrotron were reported by Stevenson et al. (2010), and related to both qualitative and quantitative X-ray imaging/tomography studies with a (filtered) white beam. The present paper reports the first results of quantitative tomography experiments conducted on the IMBL with monochromatic X-rays.

The beginning of 'tomography' is generally associated with the landmark paper of Radon (1917), although it could be argued otherwise. Tomography is not of course confined to X-rays and indeed can be said to go from 'A' (atom-probe tomography, e.g. Miller, 2000) to 'Z' (Zeeman–Doppler

tomography, e.g. Donati et al., 2008). X-ray tomography is, however, certainly the most prevalent and well known of these techniques. The origins of practical approaches to X-ray tomography, in the form of working prototypes, can be traced back to the 1930s [e.g. Vallebona (1931), Ziedses Des Plantes (1932) and Kieffer (1938) in connection with 'stratigraphy', 'planigraphy' and 'laminagraphy', respectively] and others had applied for patents as early as 1921. 'Computed tomography' (CT) was developed by Sir Godfrey Hounsfield in 1972, while working as an engineer at EMI laboratories in England, and independently by physicist Allan Cormack, for which they shared (equally) the 1979 Nobel Prize in Physiology or Medicine [see, for example, Hounsfield (1973) and Cormack (1964)]. The first commercial CT system from a major medical

equipment company (Siemens) appeared on the market in May 1974.

Reconstructed CT images are in reality maps of the linear absorption coefficient μ. However, this information is often expressed, especially for medical applications, in terms of the CT number, specified in Hounsfield units (HU). We will employ the following definition,

$$\text{CT number} = \frac{\mu - \mu_{\text{water}}}{\mu_{\text{water}} - \mu_{\text{air}}} \times 1000, \qquad (1)$$

so that water has a value of 0 HU and air -1000 HU, independent of X-ray energy E. The CT number can also be expressed, in the same basic form as (1), with μ replaced by β, the imaginary component of the complex X-ray refractive index,

$$n = 1 - \delta - i\beta, \qquad (2)$$

where $\mu = 4\pi\beta/\lambda = 2k\beta$ and the phase shift per unit length $\varphi = -2\pi\delta/\lambda = -k\delta$, with λ being the X-ray wavelength and k the vacuum wavenumber ($E = hc/\lambda$, with h being Planck's constant and c the speed of light).

Manufacturers of medical CT equipment do not usually recommend using measured CT-number values as a basis for differentiating healthy and diseased tissue, and improving the accuracy of CT numbers is an ongoing challenge [see, for example, Merritt & Chenery (1986) and Hsieh (2009)]. To illustrate the potential, for example, Albert et al. (1984) have studied the reliability of using CT numbers in the diagnosis of Alzheimer's disease. Rho et al. (1995) have investigated the relationship of mechanical properties with CT number and density for human bone, and Nuzzo et al. (2002) have used synchrotron-based tomography to obtain quantitative measurements of the degree of bone mineralization. In other fields too, the accuracy of CT numbers can be of considerable importance, for example in geology for quantitative studies of sediment cores (Orsi et al., 1994) and for the discrimination of certain mineral phases in complex systems (Tsuchiyama et al., 2005), in environmental science for testing the impact of ground water on waterproof membranes (Yang et al., 2010a), and in materials science for 'data-constrained modelling' approaches to predicting compositional microstructures (Yang et al., 2010b). A key aspect of such studies is the non-destructive nature of X-ray tomography. One cannot in general, unfortunately, make the analogous statement for medical CT as this technique does involve a relatively high radiation dose to the patient. The undoubted benefits of medical CT must therefore be balanced against the inherent risks involved and the debate continues as to what protocols should be adopted [see, for example, Golding & Shrimpton (2002) and McNitt-Gray (2002)].

In this context and in conjunction with commissioning of the IMBL, we report on the first monochromatic X-ray tomography experiments. In order to reconcile the experi-
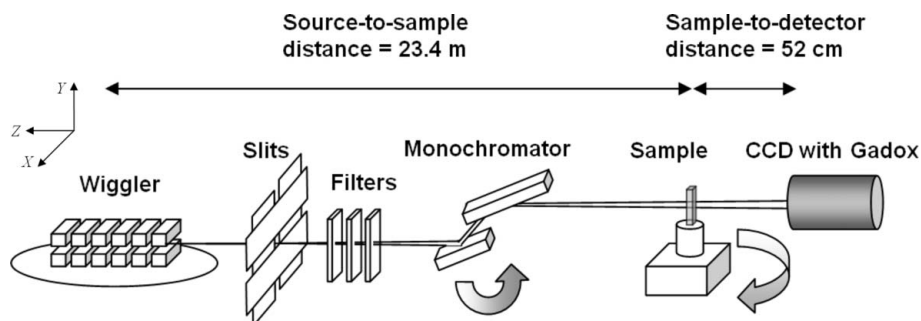

Figure 1
Schematic diagram of the experimental configuration used for the X-ray tomography experiments at IMBL. The arrow at the monochromator shows the direction of increasing Bragg angle (decreasing X-ray energy), and the arrow at the sample shows the direction of positive rotation for tomography acquisition.

mentally determined CT-number values with theoretical values we consider a number of effects including phase-contrast effects, the point-spread function (PSF) for the X-ray imaging system, and harmonic contamination of the X-ray beam. Given the increasing emphasis being placed on using X-ray tomography for quantitative, rather than just qualitative, materials characterization in a range of disciplines, it is timely that we present a comprehensive and objective assessment of those factors which need to be considered.

2. Experimental

X-ray tomography experiments were performed in the IMBL's second hutch (1B), with a source-to-sample distance (R_1) of 23.4 m and a sample-to-detector distance (R_2) of 52 cm [experimental magnification $M = (R_1 + R_2)/R_1 = 1.022$]. A schematic diagram of the experimental configuration is shown in Fig. 1. The current insertion device is an Advanced Photon Source (APS) type A permanent-magnet wiggler, with 28 × 8.5 cm periods (total length 2.4 m), which was operated with a gap of 25 mm. The field is approximately 0.838 T, the deflection parameter K is 6.65 and the critical energy E_c is 5.0 keV (see Lai et al., 1993; http://www.aps.anl.gov/Science/Publications/techbulletins/content/files/aps_1401727.pdf).[1] The RMS electron beam size in the straight sections at the Australian Synchrotron is 320 μm horizontally and 16 μm vertically (1% coupling), with a distributed dispersion of 0.1 m. These values correspond to Gaussian FWHMs of 754 μm and 38 μm, respectively. The electron-beam deviation caused by the field of the APS wiggler is small in comparison with the electron-beam size and so it is the latter which dictates the X-ray source size [see also Stevenson et al. (2010)]. The synchrotron was operated at 3 GeV and 200 mA during the present experiments, with beam decay to about 150 mA in the 12 h between injections. The X-ray beam was filtered by, allowing for all filters, windows (including for ionization chambers) and beam paths: $0.5\sqrt{2} + 0.35 = 1.06$ mm

---

[1] Magnetic field measurements performed for this wiggler (14.5, 15.5 and 23.0 mm gaps) in July 2006, prior to shipping to Australia, suggest that a field value of 0.78 T might be more accurate, for a gap of 25 mm. In this case $K = 6.2$ and $E_c = 4.7$ keV.

research papers

Be; $1.5\sqrt{2} = 2.12$ mm graphite; $0.5\sqrt{2} = 0.707$ mm Al; 1 mm kapton; 2 m He; 2.5 m air. The appearance of the factor $\sqrt{2}$ here reflects the fact that these filters were at 45° to the X-ray beam (in the horizontal plane) in the in-vacuum filter vessels in hutch 1A.

A float-zone Si monolithic $(+,-)$ double-crystal monochromator was used (in hutch 1B; 21.6 m from the source) with a vertical plane of diffraction; the doubly diffracted X-ray beam being horizontal and higher than the incident beam. This monochromator is part of a diffraction-enhanced imaging system which has been transferred to Monash University, for use at the IMBL, from Daresbury SRS (station 9.4). The first crystal face is water cooled and approximately 11 cm wide (across the X-ray beam) by 8 cm long (parallel to the X-ray beam, when Bragg angle $\theta_B = 0°$), and 27 mm thick. When $\theta_B = 0°$ there is a 5 mm gap between the first and second crystal faces in the vertical direction, and no gap in the direction of the X-ray beam, and the second crystal face (10 mm thick and the same width as first face) is approximately 12 cm long (parallel to the X-ray beam). The two, symmetric, Si 111 Bragg reflections were used to select four X-ray energies: 12.66, 18.00, 25.52 and 30.49 keV. The calibrations of the angular position of the monochromator for each of these X-ray energies was achieved by scanning through the K-edge of Se, Zr, Ag and Sb filters, respectively, and monitoring the signal with an ionization chamber.

The CCD system used was a 20 MHz 12-bit VHR2 32M camera supplied by Photonic Science. The camera design incorporates multi-stage Peltier cooling, secondary air cooling, and was operated at 258 K for these experiments. The CCD system has a single (P43) Tb-doped Gadox (gadolinium oxysulphide) input phosphor [surface density (also known as 'phosphor concentration') $\rho_s = 10$ mg cm^{-2}] viewed by two separate chips, each with 4872×3248 (horizontal $\times$ vertical) 12 µm pixels, via lenses and plane mirrors. The CCD control software performs the 'stitching' of the two individual images and corrects for barrel distortion associated with the lenses, yielding a final single image which has 8800×3100 (horizontal $\times$ vertical) pixels. In fact, all of the X-ray images recorded in the present study were restricted to an area associated with just one of the CCD chips. These images were pre-processed in conjunction with flat-field and dark-current images, i.e. images without a sample and without X-rays, respectively.

The sample used for the tomography experiments was a three-component phantom comprising monofilament nylon line, Al wire and Cu wire of approximate diameters 1.2 mm, 0.83 mm and 60 µm, respectively. The three components were twisted together as shown in Fig. 2. The tomography data were collected using 0.18° steps about the vertical sample-rotation axis over 180°, i.e. 1001 individual images[2] were recorded. The flat-field images were recorded every ten steps by translating the sample out of the X-ray beam (horizontally). The exposure time per image was 1, 0.1, 0.5 and 1 s for the 12.66, 18.00, 25.52 and 30.49 keV data sets, respectively.
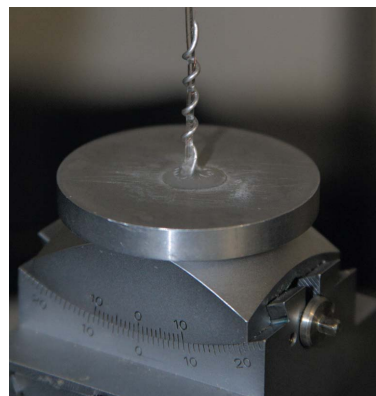

Figure 2
Three-component phantom (nylon line, Al wire and Cu wire) used for X-ray tomography experiments at the IMBL.

3. Results

Fig. 3 shows examples of pre-processed images (individual frames from each of the tomographic data sets) for the four X-ray energies used. These images are all presented on the same grey-scale range, where a normalized intensity level of 0.0 is black and an intensity level of 1.15 is white. In the absence of a sample we would have an intensity level of unity. After the initial data-processing steps had been completed, a
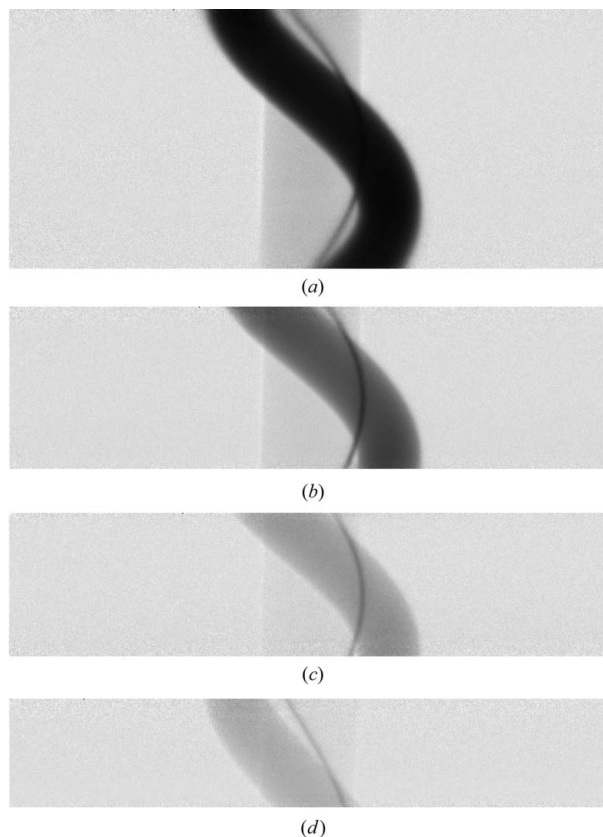

Figure 3
Examples of pre-processed X-ray images obtained for the three-component phantom at X-ray energies of: (a) 12.66 keV; (b) 18.00 keV; (c) 25.52 keV; (d) 30.49 keV. The field-of-view is 7.0 mm horizontally. Further details are provided in the text.
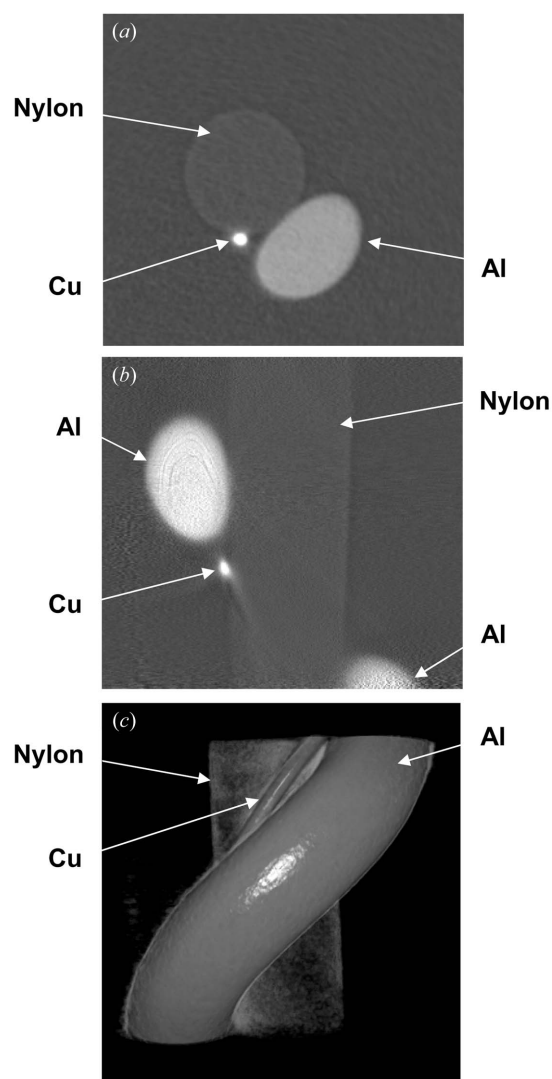
---

[2] The X-ray images were collected for a selected region-of-interest for each data set as the full CCD field-of-view was far too large.

Figure 4
(*a*) A typical reconstructed *xz* (horizontal) slice for the 25.52 keV data set; (*b*) a typical *yz* (vertical) slice for the 12.66 keV data set; (*c*) a view of the volume-rendered 12.66 keV data set. Rendering software used for (*c*): *Drishti* (Limaye, 2006).

standard parallel-beam filtered back-projection reconstruction algorithm was used for each of the four data sets. The versatile *X-TRACT* (version 4) software package (http:// ts-imaging.net/Services/) was employed for these tasks. Fig. 4 shows a typical reconstructed *xz* (horizontal) slice for the 25.52 keV data set, a typical *yz* (vertical) slice for the 12.66 keV data set, and a volume-rendered view for the 12.66 keV data set. Fig. 5 provides the experimental values of CT number in graphical form, and Table 1 shows the resulting average experimental values of CT number, for each of the three sample components and each of the four data sets. The size of the monochromatic X-ray beam in the vertical (*y*) direction decreases with increasing X-ray energy (as is apparent in Fig. 3) and therefore so does the number of reconstructed (*xz*) slices. The experimental CT numbers in Fig. 5 were determined by averaging reconstructed β-values in circular regions within each component region, for each slice.

Table 1
Experimental values of CT number in HU for each of the sample components and each of the X-ray energies.

Theoretical values are given in bold italics. Further details are provided in the text.

	12.66 keV	18.00 keV	25.52 keV	30.49 keV
Nylon	−255 (208)	−257 (227)	−185 (477)	−116 (691)
	−392	***−308***	***−195***	***−128***
Al	12100 (700)	11000 (400)	8250 (540)	6680 (800)
	12200	***11100***	***8340***	***6840***
Cu	19200 (1000)	57700 (3800)	55900 (3200)	57900 (4300)
	395000	***390000***	***311000***	***252000***

These circular regions were in the centre and had approximately half the cross-sectional area of each component. The error bars correspond to $\pm\sigma$, where σ is the estimated standard deviation for the average (we refer to these as 'intra-slice' errors). For reasons of clarity of presentation only every tenth error bar is shown in the graphs in Fig. 5. In the case of the Cu component, the circular regions used to determine the displayed CT-number values only contained nine data points. Even for this small set of data points it was apparent that this region encompassed a peak. We will discuss this aspect in more detail in the next section, but show the Cu CT-number values for just the central data points, for the reconstructed slices between the pairs of vertical dashed lines, in each case in Fig. 5 (see the grey 'plus' symbols; only every tenth such point is shown for clarity).

The experimental CT-number values in Table 1 are obtained by averaging all of the associated values between the pairs of vertical dashed lines in Fig. 5 (for Cu we use the values obtained from the nine data points, not the central data point alone, for reasons of consistency). The σ values in Fig. 5 can be used to obtain an overall intra-slice error in each case, and an 'inter-slice' error can also be generated when evaluating the average over the individual CT-number values associated with each slice. The errors quoted in Table 1 are the averages of the associated intra- and inter-slice errors, the former being the larger in all cases. It should be pointed out that the seemingly large errors quoted in Table 1, for nylon in particular, are in part due to the form of the numerator in (1), *i.e.* the relative errors for the CT-number values are significantly larger than those for the μ values (and the relative errors for the derived μ values are in general larger for lower-density and/or thinner materials anyway). Theoretical values of CT number, calculated using the mass-absorption-coefficient parameterizations provided by Zschornack (2007)[3], are also included in Table 1.

The experimental and theoretical values of CT number for nylon and Al in Table 1 are in excellent agreement, the differences being significantly smaller than the associated error values for each of the four X-ray energies. The nylon values are all negative and, as expected, fall in between the theoretical values for air and water. The Al values are of

---

[3] These data include total, not just photoelectric, cross-sections and also contribute to the experimental values of CT number inasmuch as they are the source of the required values of μ_{water} and μ_{air}. The composition and density of air was taken from ICRU (1989).
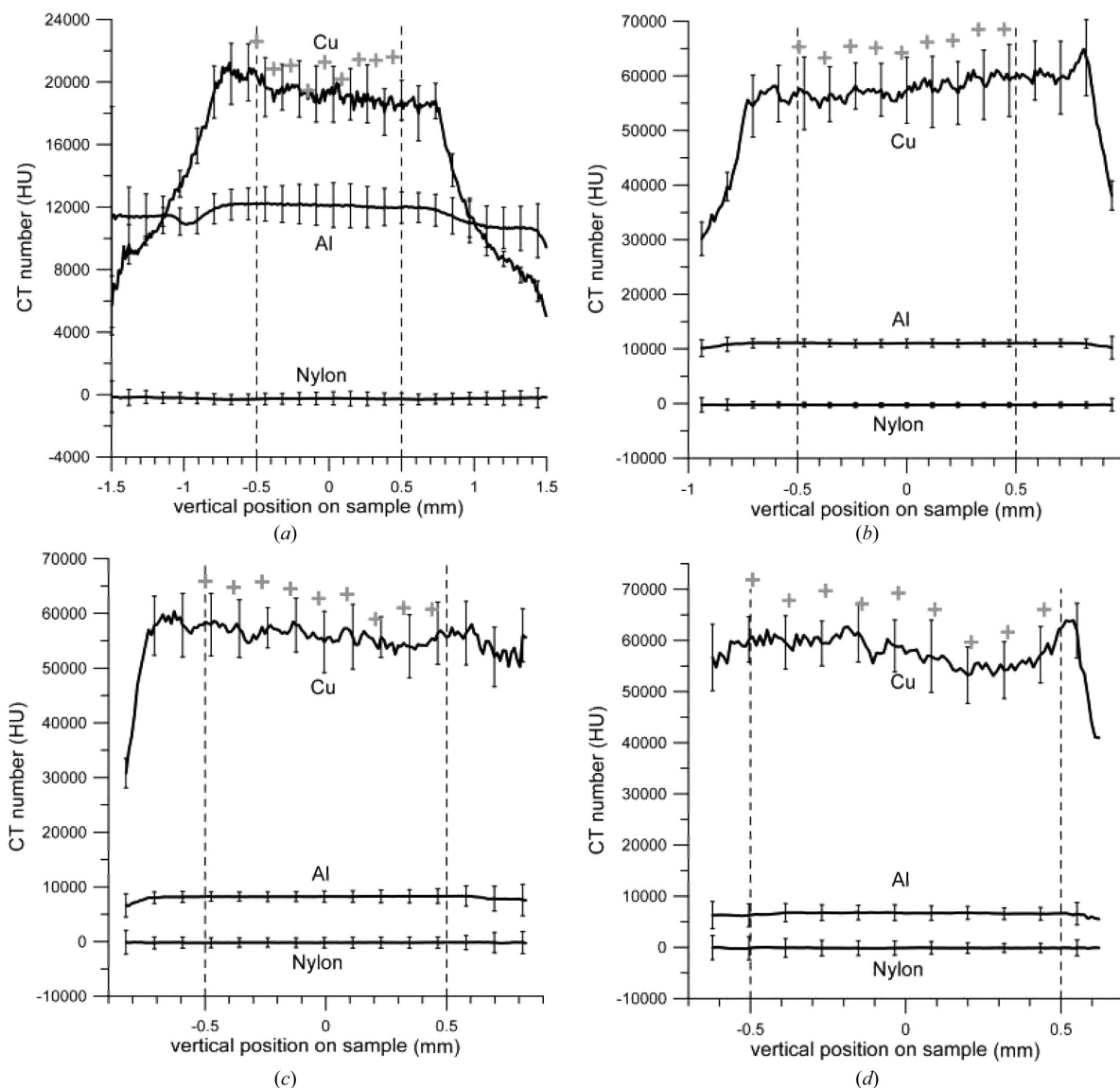
Figure 5
Experimental values of CT number as a function of vertical (y) position on the sample: (a) 12.66 keV data; (b) 18.00 keV data; (c) 25.52 keV data; (d) 30.49 keV data. Further details are provided in the text.

course considerably larger than the nylon values. The values of CT number for these two components generally decrease in magnitude with increasing X-ray energy. In stark contrast, however, there are very large discrepancies between experiment and theory in the case of Cu. The experimental values, whilst being larger than those for nylon and Al as expected, are all very much smaller than predicted. The next section (§4) is devoted to the consideration of various effects which might, at least in part, be responsible for this discrepancy.

4. Analysis

The artefacts which can occur in reconstructed tomography data are well documented, *e.g.* Barrett & Keat (2004) and Vidal *et al.* (2005). Beam hardening of polychromatic X-ray beams is a common source of tomography artefacts (such as 'cupping') and various approaches have been taken to incor-

porate corrections [see, for example, Hsieh *et al.* (2000)]. One of the key motivations for performing tomography with monochromatic X-ray beams is to avoid beam-hardening effects.

When the imaging detector used for tomography possesses individual pixels with abnormal responses, 'ring' artefacts can result, *e.g.* Sijbers & Postnov (2004). In cases where the amount of data collected is insufficient (either within individual projections or as a result of there being too few projections), 'aliasing' artefacts or streaks can occur, *e.g.* Galigekere *et al.* (1999). This 'undersampling' can be quantified *via* the Nyquist–Shannon sampling theorem (Nyquist, 1928; Shannon, 1949). Streaking can also occur as a result of sample movement, *e.g.* Yang *et al.* (1982). 'Bright-band' artefacts can occur in reconstructed data at peripheral positions when regions of the sample extend outside of the field-of-view during the tomography scan, *e.g.* Ohnesorge *et al.* (2000). Another

common artefact is the so-called 'partial volume effect' [see, for example, Glover & Pelc (1980)], where sharp boundaries between two dissimilar materials can appear blurred (such as a case for which $\mu_1 t_1 \simeq \mu_2 t_2$ but $\mu_1 \gg \mu_2$ and $t_1 \ll t_2$, where t is the thickness and the subscripts denote the two materials).

X-ray scatter can be a very significant effect in conventional cone-beam X-ray tomography and is a well known cause of artefacts, e.g. Siewerdsen & Jaffray (2001). It can also have a pronounced impact on the derived values of CT number, e.g. Joseph & Spital (1982). Kyriakou et al. (2008) have recently performed a detailed comparison of coherent and incoherent scattering contributions in the medical context, via a hybrid (analytical/Monte Carlo) simulation model. However, in the present (synchrotron, parallel-beam) case, with an incident X-ray beam of very low divergence, the effects of scatter, whilst still worthy of consideration, are reduced. As already mentioned, the mass absorption coefficients used for calculations in the present work (Zschornack, 2007) are based on total, not just photoelectric, interaction cross-sections.

We have carefully considered various artefacts, including those discussed above, in respect of the discrepancies in Table 1 (results for Cu) but cannot reconcile such effects with the nature and magnitude of differences between experiment and theory. One additional artefact type which can arise is radial streaking emanating from isolated highly absorbing features in the sample; these are sometimes referred to as 'starburst' artefacts. In the clinical context such artefacts often occur at the site of joint implants, dental fillings, metal electrodes in cochlear implants, or pace-makers. Some methods or algorithms for reducing starburst artefacts have been developed [see, for example, Glover & Pelc (1981) and Robertson et al. (1988)]. Thus far, starburst artefacts, at the site of the Cu wire, have only appeared to a quite minor extent [see, for example, Fig. 4(b)]. We will, however, return to the issue of starburst artefacts in §5. It has been implicit in our analysis of the experimental tomography data that, whilst phase-contrast effects may be present, they will not significantly affect the derived values of CT number. In the following subsection (§4.1) we will discuss the validity of this hypothesis.

4.1. X-ray phase-contrast effects

A detailed discussion of phase-contrast effects is beyond the scope of the present study; however, some consideration of the role of propagation-based phase contrast in the tomography data collected here is timely. Propagation-based phase-contrast imaging (PB-PCI) was first demonstrated and discussed in the laboratory context by Wilkins et al. (1996), and with synchrotron radiation by Snigirev et al. (1995). PB-PCI is typically characterized by its ability to provide improved contrast for weakly absorbing features and, being a differential technique[4], its enhancement of edge features. The advantages of using PB-PCI in laboratory-based tomography have been described by, for example, Mayo et al. (2003) and

Donnelly et al. (2007), and in synchrotron-based tomography by, for example, Spanne et al. (1999) and Rustichelli et al. (2004). Bronnikov (2002) and Gureyev et al. (2006) have detailed tomographic reconstruction algorithms for PB-PCI which incorporate the phase-retrieval step. The X-TRACT software used here is also capable of performing phase retrieval with a number of different algorithms, although this was not undertaken in connection with the results reported in §3. Phase retrieval also has the property of reducing the influence of noise, thereby enhancing the tomographic reconstruction results.

The two-dimensional X-ray wavefunction in the spherical-wave case can be obtained, after making certain small-angle approximations, from the Fresnel–Kirchhoff formula (Cowley, 1975; Snigirev et al., 1995) as

$$\psi_s(x, y) \simeq \frac{i}{\lambda} \int_{-\infty}^{\infty} \int_{-\infty}^{\infty} \frac{\exp\left[-ikR_1\left(1 + \frac{X^2+Y^2}{2R_1^2}\right)\right]}{R_1} q(X, Y)$$
$$\times \frac{\exp\left[-ikR_2\left(1 + \frac{(X-x)^2+(Y-y)^2}{2R_2^2}\right)\right]}{R_2} dX\, dY, \quad (3)$$

where (X, Y) are coordinates in the sample plane and (x, y) in the image plane. $q(X, Y)$ is the sample transmission function, including both absorption and phase (or refraction) effects,

$$q(X, Y) = \exp\left[-\frac{[\mu t](X, Y)}{2} - i[\varphi t](X, Y)\right], \quad (4)$$

where t is the sample thickness; if there is no sample $q(X, Y)$ is unity for all (X, Y) and (3) takes a considerably simpler form. The two-dimensional intensity distribution $I_s(x, y)$ (i.e. the X-ray image) can be obtained in the usual manner, from $\psi_s^* \psi_s$. Unfortunately, analytical solutions for $I_s(x, y)$ cannot in general be obtained, even for samples with simple geometry. However, it is quite straightforward to use a technique such as Gauss–Legendre quadrature, and, if we recognize that (3) is in fact a two-dimensional convolution, solutions can readily be obtained by using fast-Fourier transforms. It is also possible to take advantage of the simpler formulae which result for the analogous plane-wave case [to yield $I_p(x, y)$], as a straightforward transformation between $I_s(x, y)$ and $I_p(x, y)$ can readily be derived.

If we consider the case of a sample transmission function which is independent of Y (such as for a straight edge parallel to Y), it can be shown that, for a weak pure phase sample (Pogany et al., 1997),

$$I_p(x) \simeq 1 + 2\Im^{-1}\left(\Im\{[\varphi t](x)\} \sin(\pi\lambda R_2 u^2)\right), \quad (5)$$

where $\Im$ represents a Fourier transform and u is the associated variable in Fourier space. If the argument of the sin term in (5) is sufficiently small it can be shown that

$$I_p(x) \simeq 1 - \frac{\lambda R_2}{2\pi} \nabla_x^2 \{[\varphi t](x)\}. \quad (6)$$

Using the approach of Guigay (1977) [see also Guigay et al. (1971)] it can be shown that, in the case of a pure (but not necessarily weak) phase sample, (5) is actually valid for

---

[4] Wilkins et al. (1996) showed that, to a first approximation, the image structure for a pure phase sample depends on the Laplacian of the projected electron-number density $\nabla_{x,y}^2 \int \rho_e(x, y, z)\, dz$.

$|[\varphi t](x) - [\varphi t](x - \lambda R_2 u)| \ll 1$, which is less restrictive than the more usual, weak-phase, condition $|[\varphi t](x)| \ll 1$.

In the case of a pure phase sample represented by a Gaussian-blurred edge the X-ray image will typically have a characteristic black–white fringe and we can use (5) to obtain

$$I_p(x) = 1 - 2\varphi t \lambda R_2 \int_0^\infty u\, \mathrm{sinc}(\lambda R_2 u^2) \exp\left(-2\pi^2 \sigma_b^2 u^2\right)$$
$$\times \sin(2\pi u x)\,\mathrm{d}u, \tag{7}$$

where σ_b is the standard deviation for the (normalized) Gaussian, and $\mathrm{sinc}(\eta) = \sin(\pi\eta)/(\pi\eta)$, i.e. the normalized version of the sinc function. The integral in (7) cannot be solved analytically: if the approximation made in obtaining (6) from (5) is also applied in (7), the sinc term will be unity and

$$I_p(x) \simeq 1 - \frac{\varphi t \lambda R_2 x}{(2\pi)^{3/2}\sigma_b^3} \exp\left(-\frac{x^2}{2\sigma_b^2}\right). \tag{8}$$

Alternatively, a more reasonable approximation is to replace the sinc term by a Gaussian $\{\exp[-\lambda R_2 u^2/(2\sigma_{\mathrm{fit}}^2)]\}$; the use of a Gaussian approximation to the sinc function has been used successfully in various applications, e.g. Gaskill (1978) and Nakajima (2007).[5] The value of σ_{fit} which provides the best fit to the sinc function is 0.56 (0.01)[6] and (7) can then be solved. The result has the same form as (8) but with the following substitution,

$$\sigma_b \to \left(\sigma_b^2 + \alpha\lambda R_2\right)^{1/2}, \tag{9}$$

where $\alpha = 1/(4\pi^2\sigma_{\mathrm{fit}}^2) = 0.081$. This new term is associated with diffraction and in the current context is negligibly small. However, under some circumstances this term can be important and so we will retain it for completeness.

If we use (8) and (9) (with $\alpha = 0.081$) and convert to the spherical-wave case, we get

$$I_s(x) = 1 - \frac{\varphi t \lambda R' x}{(2\pi\sigma_b^2 + 0.16\pi\lambda R')^{3/2}} \exp\left[-\frac{\pi x^2}{(2\pi\sigma_b^2 + 0.16\pi\lambda R')}\right], \tag{10}$$

where $R' = R_1 R_2/(R_1 + R_2) = R_2/M$ is the effective propagation or 'defocus' distance ($R' \simeq R_2$ when $R_1 \gg R_2$, such as is often the case with plane-wave geometry at synchrotron sources; $R' \simeq R_1$ when $R_1 \ll R_2$, such as can be the case with spherical-

wave geometry and laboratory-based microfocus X-ray sources).

In order to include the effects of the source emissivity ('source size') and detector PSF or resolution we can convolute (10) with normalized Gaussian distributions (assuming an incoherent X-ray source). Given that (10) is with reference to the sample plane rather than the detector plane, the respective standard deviations, σ_s and σ_d, must be multiplied by the appropriate factors involving M. The final result is obtained by replacing σ_b in (10) by σ_{tot}, where

$$\sigma_b^2 \to \sigma_{\mathrm{tot}}^2 = \sigma_b^2 + \sigma_{\mathrm{sys}}^2 \tag{11}$$

and

$$\sigma_{\mathrm{sys}}^2 = (M-1)^2\sigma_s^2/M^2 + \sigma_d^2/M^2. \tag{12}$$

σ_{sys} combines the source and detector contributions and can be thought of as being associated with a 'system' PSF (referred to the sample plane).

The contrast is given by the difference between the maximum and minimum intensity values divided by their sum. The resolution is given by the difference in position between these maximum and minimum intensity values, referred to the sample plane. It can be shown using (10)–(12) that the contrast is given by

$$C = -\frac{2\varphi t \lambda R'}{\pi(2\pi e)^{1/2}(4\sigma_{\mathrm{tot}}^2 + 0.32\lambda R')}, \tag{13}$$

and the resolution by

$$R = \left(4\sigma_{\mathrm{tot}}^2 + 0.32\lambda R'\right)^{1/2}. \tag{14}$$

It must be remembered that φ is negative for X-rays and so the value of C from (13) will be positive. It should also be pointed out that the minimum and maximum intensity values (which form the characteristic black–white fringe) are disposed symmetrically about $x = 0$, with the latter being on the side corresponding to a vacuum. As expected, large values of R ('poor' resolution) accompany small values of C ('low' contrast), whereas 'good' resolution is concomitant with 'high' contrast. It is convenient to discuss the limiting cases of (13) and (14) in terms of the Fresnel number, defined as $N_F = k\sigma_{\mathrm{tot}}^2/R' = 2\pi\sigma_{\mathrm{tot}}^2/(\lambda R')$. In the 'near-Fresnel' region, where $N_F \gg 1$, $R = 2\sigma_{\mathrm{tot}}$ and $C = -0.242\varphi t/N_F$. In the 'far-Fresnel' or 'Fraunhofer' region, where $N_F \ll 1$, $R = 0.568(\lambda R')^{1/2}$ and $C = -0.477\varphi t$. These results for contrast and resolution are in excellent agreement with the corresponding ones obtained in the more comprehensive study by Gureyev et al. (2008), with the exception of the value of R in the latter case. This value is expected to be $(\lambda R')^{1/2}$, which represents the width of the first Fresnel zone, e.g. Cosslett & Nixon (1953). The discrepancy can be attributed to the approximations made, in particular the need to replace the sinc term by a Gaussian in (7). If instead we apply the conditions $N_F \gg 1$ and $N_F \ll 1$ at the outset, there is no necessity to make this substitution in either case, and the results for the 'near-Fresnel' region remain unchanged. In the case of the 'far-Fresnel' region, however, the analogous expression to (10) is then $I_s(x) = 1 - $

---

[5] The analogous expression to (7) for a Gaussian-blurred cylinder of diameter t involves multiplying the integral by $-\pi$, replacing $\sin(2\pi u x)$ by $\cos(2\pi u x)$, and including an extra factor $J_1(\pi t u)$ (the Bessel function of the first kind of order one) in the integral. Whilst there are various representations of and approximations to the Bessel function [see, for example, Gross (1995)], these do not provide an analytical solution for $I_p(x)$. The familiar series expansion, whilst converging for all values of the argument, does not start to converge until the number of terms considered is very much greater than the absolute value of the argument. If we do use this series expansion for the Bessel function, and one of the above-mentioned approximations to the sinc term, the resulting expression for $I_p(x)$ will involve a sum of integrals; these integrals can be solved analytically [see, for example, Gradshteyn & Ryzhik (1965)], with the solutions expressed in terms of Hermite polynomials, but there will still be the concomitant convergence issues.

[6] This value was determined by using a modified Levenberg–Marquardt algorithm (Levenberg, 1944; Marquardt, 1963) for solving non-linear least-squares problems, which avoids the need for explicit derivatives.

$\varphi t [F_C\{\sqrt{2}x/(\lambda R')^{1/2}\} - F_S\{\sqrt{2}x/(\lambda R')^{1/2}\}]$, where the two functions in the square brackets are the Fresnel cosine and Fresnel sine integrals. We have adopted the definitions of these transcendental functions given by, for example, Abramowitz & Stegun (1965) [rather than those of, for example, Gradshteyn & Ryzhik (1965)]. It can then be shown that $R = (\lambda R')^{1/2}$ and $C = -[F_C(1/\sqrt{2}) - F_S(1/\sqrt{2})]\varphi t = -0.488\varphi t$.

If we examine (11)–(13), neglecting the diffraction term, with $R_1 + R_2$ held fixed, it can be shown that the optimum magnification (for maximum contrast) is given by $1 + [(\sigma_b^2 + \sigma_d^2)/(\sigma_b^2 + \sigma_s^2)]^{1/2}$, which is less than 2 for $\sigma_s^2 > \sigma_d^2$, equal to 2 for $\sigma_s^2 = \sigma_d^2$, and greater than 2 for $\sigma_s^2 < \sigma_d^2$. The situation for (14), neglecting the diffraction term, is that the optimum magnification, for a minimum value of R, is $(\sigma_s^2 + \sigma_d^2)/\sigma_s^2$, which satisfies the same relationships mentioned above (in connection with the optimum magnification for maximum contrast)[7]. We will discuss the values of σ_s^2 and σ_d^2 for the present case in detail below but it suffices to point out that our value of M (1.022) is significantly smaller than the optimum value (for maximum phase contrast), especially in the vertical direction, where $\sigma_s^2 < \sigma_d^2$ (in the horizontal direction $\sigma_s^2 > \sigma_d^2$).

In the present case of course, the individual components of the phantom are neither pure phase samples nor are they blurred edges. We can, however, gain some valuable insights by considering certain 'back-of-the-envelope' calculations. For a weakly absorbing edge sample (and no phase effects), we can use the Beer–Lambert law to show that the associated absorption contrast, in analogy to (13), is simply $\mu t/2$. Whilst δ/β is often used as a convenient quantity in discussions of phase- and absorption-contrast effects, it does not itself give a convenient measure of the relative magnitudes of these two effects in X-ray images. If we take the ratio of (13), neglecting the diffraction term, and $\mu t/2$ we obtain the result $\mathcal{R} = (A/E)(\delta/\beta)$, representing the phase contrast relative to absorption contrast, where A combines various constants and depends on R_1, R_2 and σ_{tot}. If we assume that $\sigma_{tot} = 40$ μm ($\sigma_b = 0$ μm and $\sigma_{sys} = 40$ μm; this will be justified below) then $A \simeq 15$ eV, with E in units of keV. Table 2 gives values of both δ/β and $\mathcal{R}$ for each of the three sample components and each of the four X-ray energies. The source of data for calculation of β-values has already been described above. The δ-values were calculated with the aid of data from McMaster et al. (1970) and Brennan & Cowan (1992). The material properties of the components are taken to be as follows: nylon, nylon 6-6, $C_{12}H_{22}N_2O_2$, $\rho = 1.13$ g cm^{-3}; Al, $\rho = 2.698$ g cm^{-3}; Cu, $\rho = 8.960$ g cm^{-3}. None of the components has any absorption edges in the X-ray energy range covered and, based on photoelectric cross-sections alone, we would expect δ/β to vary as E^2 and $\mathcal{R}$ as E. The fact that the data follow these trends reasonably closely for Al and Cu, and show a significant departure for nylon, is due to greater importance of the other interaction cross-sections in the case of the lighter elements and higher X-ray energies. Our rather crude prediction of the

Table 2
Theoretical values of the dimensionless quantities δ/β (top rows) and $\mathcal{R}$ (bottom rows; bold italics) for each of the sample components and each of the X-ray energies.

Further details are provided in the text.

	12.66 keV	18.00 keV	25.52 keV	30.49 keV
Nylon	1260	2010	2570	2660
	1.51	*1.70*	*1.53*	*1.32*
Al	123	243	466	621
	0.148	*0.205*	*0.277*	*0.309*
Cu	12.8	23.8	44.2	61.1
	0.0154	*0.0201*	*0.0263*	*0.0304*

ratio of phase- to absorption-contrast effects in the X-ray images suggests: that we would not expect to see the former for Cu; it is marginal for Al; and there should be quite significant phase-contrast effects for nylon. Very close inspection of the pre-processed X-ray images (prior to tomographic reconstruction), such as those in Fig. 3, does suggest the presence of weak phase-contrast effects for the nylon component at each of the four X-ray energies (and not for Al and Cu). However, the more compelling such evidence comes from the actual reconstructed slices [see, for example, Figs. 4(a) and 4(b)]. This observation is in part a consequence of the 'dose fractionation theorem' (Hegerl & Hoppe, 1976; McEwen et al., 1995), but also the inherent nature of the two data forms [this will be demonstrated in the next subsection (§4.2)].

In Fig. 6 we present the results of taking radial profiles through the nylon, Al and Cu regions, for each of the four X-ray energies. These profiles have been obtained by using all of the reconstructed slices with a value of y between -0.5 mm and 0.5 mm (see the pairs of vertical dashed lines in Fig. 5). The step size for these profiles is the pixel size of the CCD, referred to the object plane, i.e. 11.74 μm. The useful range of pole angles (for which the presence of other components does not obtrude) is approximately 255° for nylon, 260° for Al, and 100° for Cu. As a result of difficulties in ascertaining the central reference position for each component, and departures from circularity of the component's cross-section (particularly in the case of Al[8]), we obtained radial profiles for sectors (nine for nylon and Al, and just one for Cu) within each reconstructed slice. These individual radial profiles were then correlated prior to averaging, to yield the final radial profile for each component. In order to obtain the positional shifts from the correlations of profiles, we first smoothed these profiles by using a 'running average' over ten data points. In the cases of nylon and Al, where the profiles start within the component itself, the correlations are actually performed with the derivatives of profiles due to the nature of curves and the need to fulfil periodic boundary conditions for the Fourier

---

[7] A more complicated set of conditions (which are too detailed to be presented here) prevail when the diffraction terms in (13) and (14) are significant.
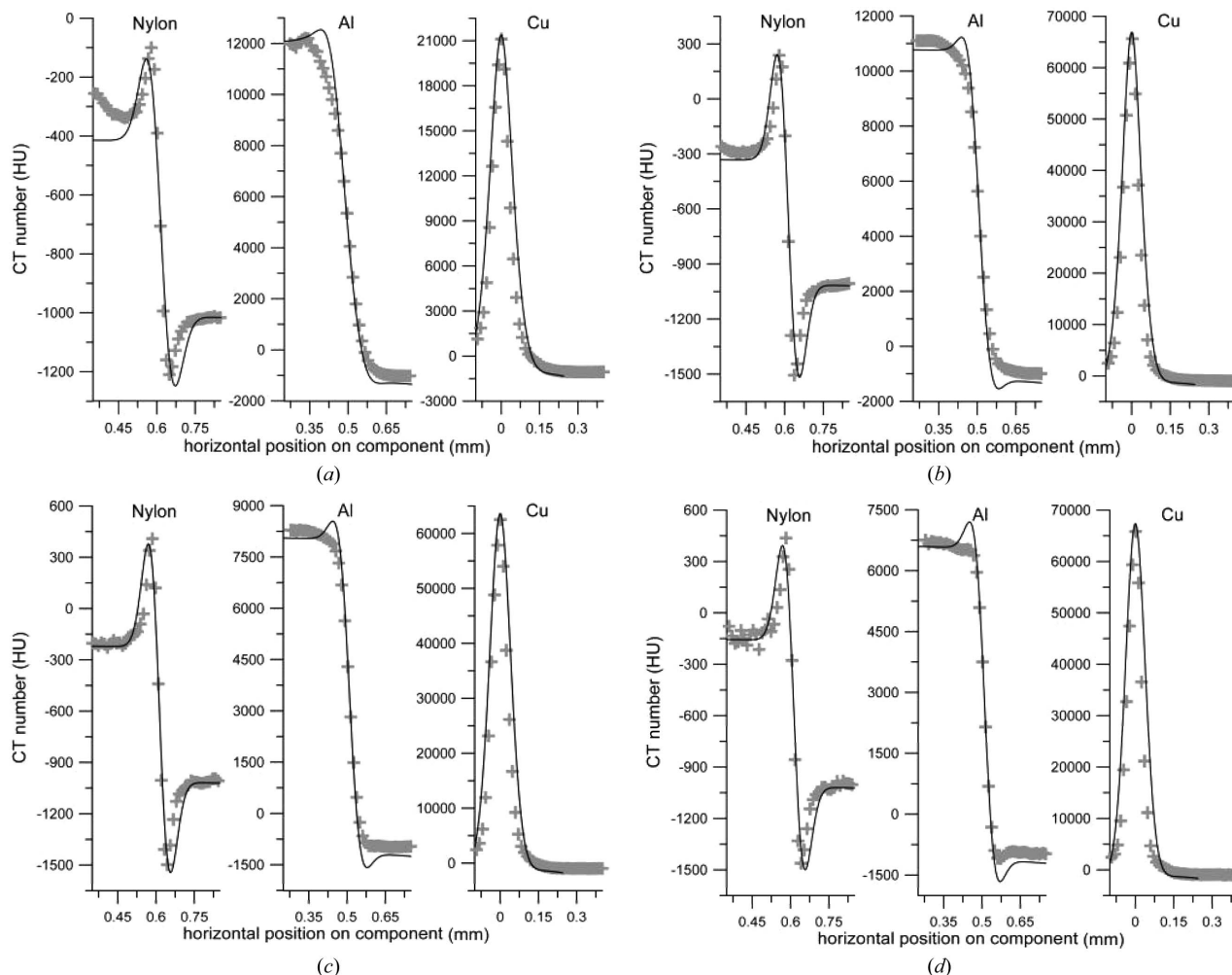
[8] Given that the nylon line is essentially parallel to the sample rotation axis and the Cu wire has such a small diameter, the Al wire is the main issue here, e.g. see Fig. 4. The typical reconstructed xz (horizontal) slice shown in Fig. 4(a) shows a rather distorted/somewhat elliptical cross-section for the Al wire. This is entirely consistent with this wire actually having a circular cross-section, when allowance is made for the 'pitch' involved (see Fig. 2).

Figure 6
Experimental values of CT number (grey data points) as a function of radial distance from the centre of each component for: (a) 12.66 keV; (b) 18.00 keV; (c) 25.52 keV; (d) 30.49 keV. Further details are provided in the text. The solid curves are the result of numerical image simulations which are discussed in detail in §4.2.

methods employed. In the Cu case the profiles encompass most of the component and the correlations can be performed without the need to take derivatives. It should be noted that the background values are very close to −1000 HU (as expected for air); see, also, more detailed discussions in the next subsection (§4.2). We also note that, as expected, the peak values for the Cu data are in excellent accord with the values in Fig. 5 (on average) which correspond to the central data points in each reconstructed slice, rather than those corresponding to an average over nine data points.

The experimental results presented in Fig. 6 show that phase-contrast effects are indeed significant for the nylon component, but not for the Al and Cu components. There is, however, a slight indication of the presence of such effects for Al [see Figs. 6(a) and 6(d) in particular]: it must also be remembered that the actual geometry of the Al wire and its associated pitch will result in these effects being, on average, reduced experimentally (and dependent on the pole angle), relative to any theoretical expectations for a truly straight cylindrical wire. The experimental values of CT number, derived using data from the central part of the component

regions and avoiding the edges, will not, in any event, be affected by phase-contrast effects and, in particular, do not provide an explanation for the discrepancy between theory and experiment for the Cu data. The Cu results presented in Fig. 6 do, however, suggest that the role of the system PSF should be investigated.

4.2. The role of the point-spread function

The profiles shown in Fig. 6 may provide an important clue as to the source of the discrepancy for Cu. In the case of nylon we have a flat plateau in the centre and the distinctive black–white fringe associated with phase contrast at the edge; for Al, just the plateau; and for Cu, a highly peaked, almost triangular distribution. In the absence of phase-contrast effects we would expect a PSF whose width is small compared with the diameter of the component, to have the effect of 'rounding the corners' of the top-hat-like CT-number profile, as exemplified by the Al results. However, if the width of the PSF is comparable with that of the component, a distribution such as that obtained with the Cu results may well be produced.

The system PSF, as given by (12), is dependent on the X-ray source emissivity distribution (essentially the source size) and the detector resolution. The PSF has already been shown to be important in connection with PB-PCI and we will show in this section that it is of more general significance. The nominal X-ray source size in the current context is 320 µm horizontally [σ_s (horiz)] and 16 µm vertically [σ_s (vert)]; Stevenson *et al.* (2010) determined the former to be 346 (14) µm, in good agreement with the nominal value. We will use the latter value of σ_s (horiz) and the nominal value of σ_s (vert) in our further analysis of the experimental tomography data.

Stevenson *et al.* (2010) determined the value of σ_d to be 19.2 (0.5) µm for a Photonic Science 10 MHz 16M FDI-VHR CCD camera with a (P43) Tb-doped Gadox phosphor (5 mg cm^{-2}) and 7.4 µm pixels. The CCD for the present study (described in §2) is from the same manufacturer and has ρ_s = 10 mg cm^{-2} phosphor and 12 µm pixels. The thickness of the phosphor can be calculated using the formula $\rho_s = \rho p t_{Gadox}$, where ρ is the (bulk) density and p is the packing fraction; for Gadox ρ = 7.34 g cm^{-3} and p is typically close to 0.5 [see, for example, Graafsma & Martin (2008)], giving t_{Gadox} = 27 µm. A number of rules-of-thumb have been suggested for CCD resolution [see, for example, Meyer (1998)] and a common theme is that they involve a linear combination of phosphor thickness (the grain size can also be a significant factor) and pixel size. Given that, assuming the same packing fraction, the phosphor for the CCD used here will be twice the thickness of that used by Stevenson *et al.* (2010) and that the pixels are also roughly twice the size (12 µm/7.4 µm ≃ 1.6), it is reasonable to assume that σ_d = 2 × 19.2 µm = 38.4 µm for the present study. Thus the value of $M\sigma_{sys}$ (horiz) would be 39.2 µm [using (12)] and for $M\sigma_{sys}$ (vert) 38.4 µm, and hence the adoption of a two-dimensional Gaussian PSF (referred to the detector plane, hence the inclusion of the factor M) with $M\sigma_{sys}$ = 40 µm both vertically and horizontally is a reasonable starting point for this study. It should be noted that we are able to treat σ_{sys} (horiz) and σ_{sys} (vert) as being equal to a good approximation because M is very close to unity in the present case and so the associated large demagnification of the X-ray source ensures that the PSF is dominated by the (isotropic) detector resolution, *e.g.* if M were increased to 1.2 we would have $M\sigma_{sys}$ (horiz) = 79.1 µm and $M\sigma_{sys}$ (vert) = 38.5 µm, with the anisotropic source size having a significant impact.

Stevenson *et al.* (2010) did, however, point out that the value they obtained for σ_d was larger than expected and may reflect that 'some factor not accounted for in our model is causing an apparent degradation of the detector resolution'. This factor could, for example, be the result of extraneous X-ray scatter reaching the CCD. It would therefore seem prudent to consider the detector resolution for the current CCD detector in more detail. To this end we collected X-ray images (at 20 keV) for a Leeds type 18d line-pair phantom placed on the front of the CCD, thereby ensuring that the effect of the source size is negligible and reducing the effects of any unwanted scatter. This phantom has a range of periodic line structures from 1.0 to 20.0 line-pairs mm^{-1}, with the lines being 30 µm-thick Pb (the transmission for which is approxi-
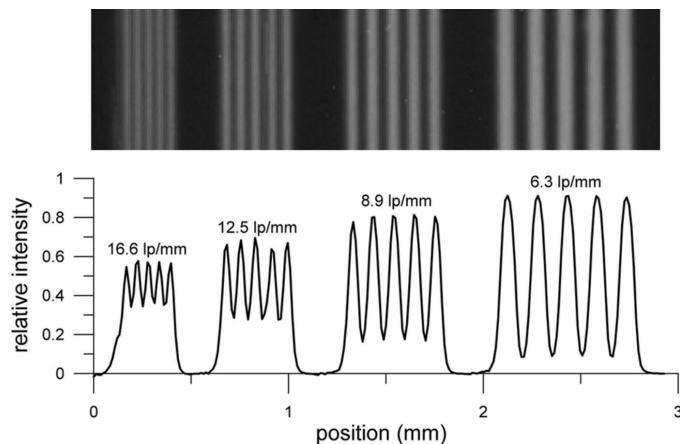

Figure 7
X-ray image (20 keV) and corresponding profile for a line-pair phantom.

mately 5% at 20 keV). Fig. 7 shows part of one of these X-ray images, plus the profile through the periodic structures.

If we represent the line-pair periodic structures by a square wave which varies from 0 to 1 and has period T, we can use the Fourier-series expansion and convolute term-by-term with a line-spread function (LSF)[9]:

$$\frac{1}{2} + \frac{2}{\pi}\sum_{n=1}^{\infty} f\left[\frac{(2n-1)\pi w}{T}\right]\sin\left[\frac{2(2n-1)\pi x}{T}\right]/(2n-1), \quad (15)$$

where w is the FWHM for the LSF and

$$f[\eta] = \exp\left[-\eta^2/(4\ln 2)\right], \quad (16a)$$

$$f[\eta] = \exp(-\eta) \quad (16b)$$

or

$$f[\eta] = \sin(\eta)/\eta. \quad (16c)$$

Equations (16a), (16b) and (16c) apply, respectively, to a normalized Gaussian LSF [$w = (8\ln 2)^{1/2}\sigma$], a normalized Lorentzian (Cauchy) LSF and a normalized top-hat LSF. It should be noted that in the case of a Gaussian or a top-hat LSF, PSF(x, y) = LSF(x)LSF(y), the PSF has the same functional form (in two dimensions) as the LSF (in one dimension), and the associated widths are the same in x and y. These statements do not hold for a Lorentzian LSF; its inclusion in our analysis was thought to be important, however, as scattering effects within the CCD phosphor and beyond often lead to PSFs with long 'tails' [see, for example, Naday *et al.* (1994)]. Consideration of more general functional forms for the LSF or PSF is beyond the scope of the present study but it is worth pointing out that a Pearson VII function (Pearson, 1916) [often used to describe powder-diffraction peak profiles (both X-ray and neutron); see, for example, Hall *et al.* (1977)] may well merit investigation. Such a PSF can be written as

$$\text{PSF}(x, y) = \text{PSF}(0, 0)\left[1 + \frac{4(x^2 + y^2)}{w'^2}\right]^{-\tau}, \quad (17)$$

---

[9] To be rigorous we refer here to the line-spread function, which is the 'projection' (see later in this section) of the two-dimensional PSF onto one dimension.

where w' is related to the width [the FWHM is given by $w'(2^{1/\tau} - 1)^{1/2}$, which is equal to w' when $\tau = 1$], and τ is a shape factor, largely responsible for the rate at which the function's tails will decrease. Interestingly, (17) is used quite extensively to describe stellar images in astronomy and is known as the (circular) Moffat function (Moffat, 1969); in this field τ is known as the 'atmospheric scattering coefficient'. If $\tau = 1$, (17) is a Lorentzian and, in the limit of $\tau \to \infty$, a Gaussian results [see, for example, Trujillo *et al.* (2001)]. In between these extremes we have the 'intermediate' Lorentzian ($\tau = 1.5$) and the 'modified' Lorentzian ($\tau = 2$) [see, for example, Young & Wiles (1982)].

We can obtain experimental values of the peak-to-trough ratio for each line-pair structure from the X-ray images and then compare these with the results of calculations using (15), (16a), (16b) and (16c). In performing the calculations we used $N = 100$ terms in the summation in (15) in order to ensure that the approximation to the original square wave was accurate. In addition, we have included an extra factor in the summation, sinc$\{(2n - 1)/[2(N + 1)]\}$, which is often referred to as a Lanczos σ factor (Lanczos, 1956) and has the effect of mitigating the ringing artefacts which can occur at the 'corners' of the square wave [such artefacts are usually referred to as the 'Gibbs phenomenon'; see Gibbs (1898, 1899)]. The experimental peak-to-trough ratios for the four line-pair structures in Fig. 7 are, from left to right, 1.5, 2.3, 4.8 and 11. If we perform calculations based on a Lorentzian LSF [(15) and (16b)] the four values of w are, from left to right in Fig. 7, 36, 29, 21 and 13 μm, *i.e.* there is quite poor consistency. In the case of a top-hat LSF [(15) and (16c)] the values are 51, 58, 68 and 87 μm, which also show rather poor agreement. Finally, for the Gaussian LSF [(15) and (16a)], the values are 44, 46, 49 and 53 μm, which may still display some systematic trend, but are certainly the most consistent. We might, rather simplistically, suppose that the most appropriate LSF is somewhere in between a Lorentzian and a Gaussian, and closer to the latter. If we adopt the Gaussian LSF (and therefore PSF) results, the average of the associated w-values is 48 (4) μm and we have a value of σ_d of 20 (2) μm.[10] In this case, for the tomography experiment, $M\sigma_{sys}$ (horiz) = 21 μm and $M\sigma_{sys}$ (vert) = 20 μm; thus $M\sigma_{sys} = 20$ μm both vertically and horizontally represents the smallest PSF which it would be reasonable to consider in the present study.

We will now proceed to describe the results of numerical simulations undertaken with a view to better understanding the remaining discrepancy between theory and experiment in respect of CT numbers, *i.e.* the Cu results in particular. We will use (3) and (4) to calculate X-ray images with the experimental conditions already described and then convolute these with two-dimensional Gaussian PSFs, referred to the detector plane ($M\sigma_{sys}$ with a typical value of 40 μm, and a minimum value of 20 μm; remembering that σ_{sys} is referred to the sample plane). These images are then used to form simulated

tomographic data sets, which can be subjected to the same reconstruction procedures as applied to the original experimental data. We have experimented with different amounts of Poisson-distributed noise in the original calculated images and, whilst the reconstructed data display the effects of this noise, there was no significant difference in the derived values of the average CT number apart from in the associated estimated standard deviations (e.s.d.s), as expected.

In the case of a cylinder we cannot assume that any Gaussian blur which we might wish to include, as characterized by σ_b, can be simply added to σ_{sys} in quadrature [as was the case in (11) for a Gaussian-blurred edge]. In the context of (4) we consider the pathlength $t(X, Y) \equiv t(X)$, for a cylinder whose axis is vertical (parallel to Y), to be given by

$$t(X) = \int_{-\infty}^{\infty} S(X, Z)\,\mathrm{d}Z, \tag{18}$$

where the Z-axis is (anti-)parallel to the optic axis or X-ray beam direction, and $S(X, Z)$ is a mask with a value of 0 outside the cylinder and 1 inside the cylinder. If there is no blurring of the cylinder, $S(X, Z)$ is simply a filled circle of diameter t and $t(X)$ is 0 for $|X| > t/2$ and $(t^2 - 4X^2)^{1/2}$ for $|X| \leq t/2$. When $S(X, Z)$ is convoluted with a (normalized) two-dimensional Gaussian and then (18) is used we obtain curves such as those in Fig. 8.[11] We have normalized both axes (and σ_b) by t so that the curves are in some sense 'universal'. It is worth noting that we are implicitly assuming the validity of the 'projection approximation' [see, for example, Paganin (2006)], and Morgan *et al.* (2010) have recently provided a detailed consideration of this approximation in the context of PB-PCI for a cylinder edge. Based on our experience with other phantoms we have chosen to use $\sigma_b = 5$ μm for each of the three components being considered. This value is reasonable for these cylindrical components and the accuracy of σ_b is not critical here as its role is subsidiary to that of σ_{sys}.

---

[10] Compare with one of the most frequently employed rules-of-thumb for detector resolution alluded to above, that the FWHM resolution is twice the pixel size plus half the phosphor thickness, *i.e.* $\sigma_d = 16$ μm in the present case.

[11] We can think of (18) as defining a 'projection' of $S(X, Z)$ onto one dimension to yield $t(X)$. It can be shown that, when $S(X, Z)$ is to be convoluted with a two-dimensional blurring function, an equivalent approach to obtaining $t(X)$ is to 'project' these two two-dimensional functions and then convolute the resulting one-dimensional functions, *i.e.* the convolution and projection operations commute [see, for example, Natterer (2001)]. The projection of a two-dimensional Gaussian can easily be shown to be a one-dimensional Gaussian, and similarly the projection of a two-dimensional top-hat distribution is a one-dimensional top-hat distribution. The case of a two-dimensional Lorentzian, however, is not as straightforward: firstly, the (double-)integral of a two-dimensional Lorentzian over all of X–Z space diverges and so the function cannot be normalized; secondly, whilst the integral arising from the application of (18) is otherwise easily evaluated, the resulting one-dimensional function is not a Lorentzian. The first point is borne out by the fact that, in order to normalize the function in (17), it can be shown that PSF$(0,0) = 4(\tau - 1)/(\pi w'^2)$; this result is only valid for $\tau > 1$, a condition imposed in solving one of the integrals involved (see Gradshteyn & Ryzhik, 1965): thus for a Lorentzian, where $\tau = 1$, (17) cannot be normalized. On the second point, the application of (18) to an 'intermediate' two-dimensional Lorentzian produces a one-dimensional Lorentzian, and for a 'modified' two-dimensional Lorentzian we get a one-dimensional 'intermediate' Lorentzian. Put more generally (the validity condition here is $\tau > 1/2$), the projection, as defined in (18), of a two-dimensional Pearson VII function with shape factor τ will be a one-dimensional Pearson VII function with shape factor $\tau - 1/2$, and this statement still holds in the limit of $\tau \to \infty$ where a two-dimensional Gaussian is projected to a one-dimensional Gaussian as noted above.
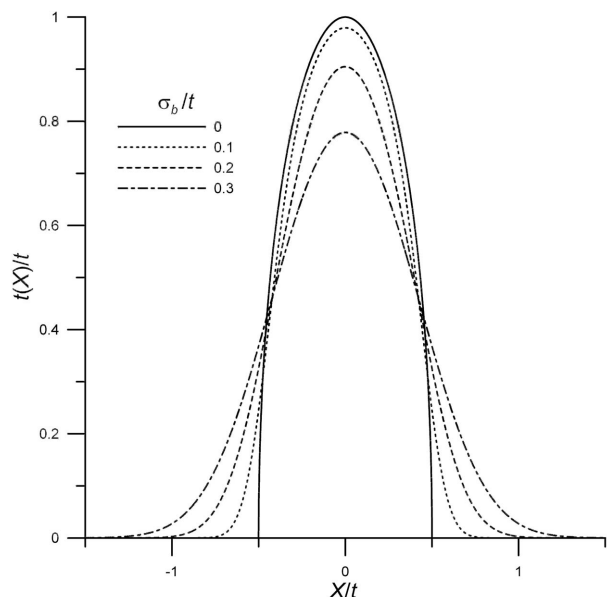
Figure 8
Pathlength as a function of lateral position on the sample for a vertical cylinder of diameter t, for different amounts of Gaussian blur (as characterized by σ_b). The quantities X, $t(X)$ and σ_b have all been normalized by t.

Fig. 9 shows results of numerical simulations for the nylon cylinder with X-rays of energy 25.52 keV. In Fig. 9(a) one-dimensional intensity profiles through the simulated two-dimensional X-ray images for different values of $M\sigma_{sys}$ are shown. Fig. 9(b) shows the corresponding CT-number profiles through a (central) reconstructed xz slice. It is quite apparent

from these profiles that the phase-contrast effects at the cylinder edges will be much easier to see in the CT-number profiles, as we have already noted for the experimental results. Close inspection of Fig. 9(b) reveals some very minor anomalous features: those parts of the curves corresponding to air are not constant at −1000 HU as expected, but have a slight slope, with a value of −1040 HU at the extremes (±1.2 mm); the value shown at 0 mm is approximately −219 HU whereas we would expect a value of −195 HU (see the theoretical value in Table 1 for nylon and 25.52 keV); taking the edges of the cylinder to be at those positions where the CT number has a value equal to the average of the values at the peak and the trough yields a nylon diameter of $t = 1.23$ mm, rather than the expected value of 1.20 mm. The measure of the cylinder-edge positions used here cannot be justified in general but is quite accurate in this case of an object which has relatively weak phase contrast. The third of these minor anomalous features provides the most obvious clue to the cause: the numerical image simulations were performed for cone-beam geometry, albeit with the magnification very close to unity, and the tomographic reconstruction was performed using a parallel-beam algorithm. The insert graph in Fig. 9(b) shows a section of the $M\sigma_{sys} = 40$ µm curve from the main graph, plus the corresponding curve for a cone-beam reconstruction (Feldkamp et al., 1984). In the latter case CT numbers in the regions corresponding to air no longer have a significant slope and the value at the extremes (±1.2 mm) is now −1007 HU; the value of CT number at 0 mm is now −199 HU; the nylon diameter is the expected $t = 1.20$ mm. That is, the minor anomalous features noted above have essentially been resolved. Finally,
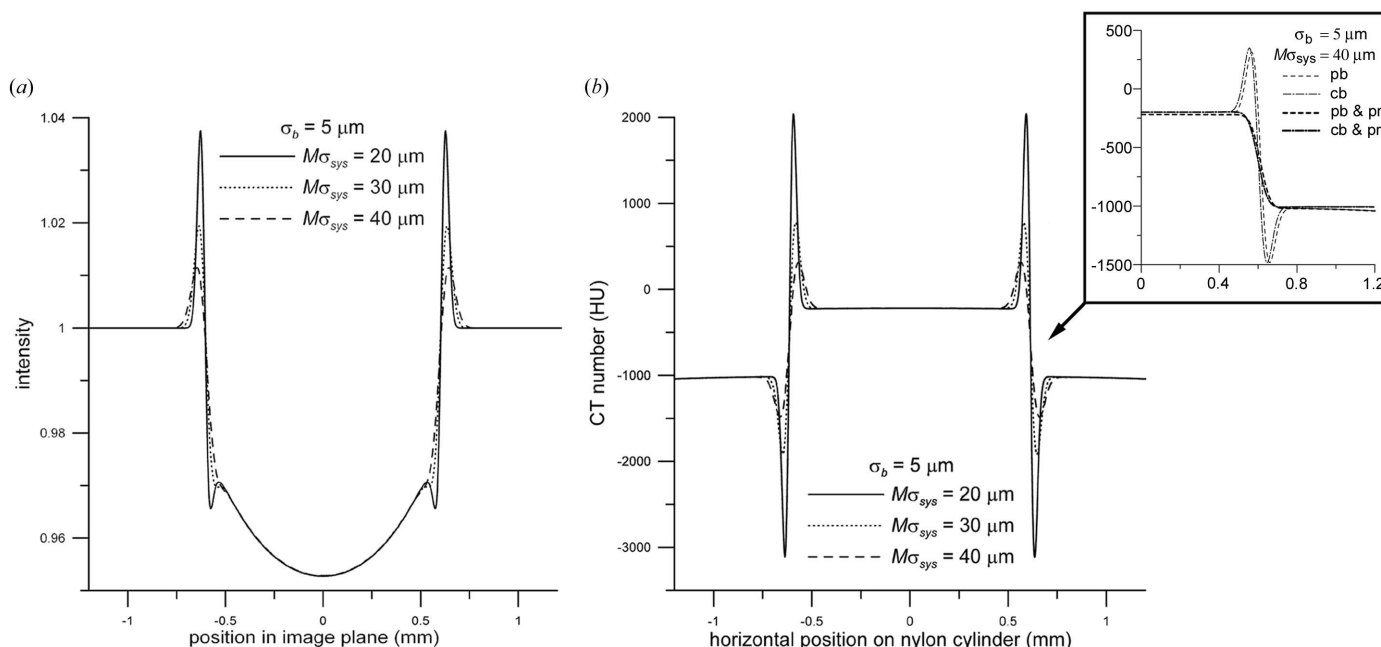

Figure 9
(a) Profiles from image simulations using the Fresnel–Kirchhoff formula for a 1.2 mm-diameter nylon cylinder and 25.52 keV X-rays. The curves correspond to different widths of the PSF. (b) CT-number profiles through a reconstructed xz slice from image simulations using the Fresnel–Kirchhoff formula for a 1.2 mm-diameter nylon cylinder and 25.52 keV X-rays. The curves correspond to different widths of the PSF. The insert graph shows expanded detail at one cylinder edge for the $M\sigma_{sys} = 40$ µm curve ('pb' denotes parallel-beam reconstruction) plus the curve for cone-beam reconstruction ('cb'), and the corresponding curves with inclusion of a phase-retrieval processing step ('pb & pr' and 'cb & pr', respectively). Further details are provided in the text.

Table 3
Values of $M\sigma_{sys}$ (µm) which provide the best agreement between the experimental and theoretical profiles in Fig. 6 for each of the sample components and each of the X-ray energies.

The values for Al are in brackets and italicized because they are just the averages of the values for nylon and Cu. Further details are provided in the text.

	12.66 keV	18.00 keV	25.52 keV	30.49 keV
Nylon	46	38	38	38
Al	*(48)*	*(39)*	*(40)*	*(38)*
Cu	50	41	43	39

the insert graph also includes the corresponding curves for the case where the original simulated images are subjected to phase retrieval prior to the formation of sinograms. This phase-retrieval step was performed using the algorithm developed by Paganin *et al.* (2002), which utilizes the 'transport-of-intensity' equation (Teague, 1983) and assumes a homogeneous object (required input parameters are $\delta/\beta = -2\varphi/\mu = 2570$ for nylon and 25.52 keV, and $R' = 50.9$ cm). In this case (see the 'cb & pr' curve) the form of the CT-number profile relates directly to the cylinder geometry, without what is essentially an artefact (the characteristic black–white fringe) resulting from phase-contrast effects. The application of this phase-retrieval algorithm to the experimental data is complicated by the fact that we have three quite distinct materials present rather than just one. As we will see below, we are able to use the phase-contrast artefacts present in the reconstructed CT-number data to considerable advantage and so we will not further pursue the use of phase retrieval here. However, the recent algorithm developed by Beltran *et al.* (2010) might well be applied to such experimental data.

Fig. 10 shows the analogous curves to those in Fig. 9, for the Cu cylinder with X-rays of energy 25.52 keV. In this case the sensitivity of the curves, and the CT-number value at the peak in particular, to the width of the PSF is quite apparent. If we vary the value of $M\sigma_{sys}$ (whilst holding σ_b fixed at 5 µm) to obtain the 'best' agreement with each of the experimental radial profiles in Fig. 6 (separately), we obtain the solid curves included in Fig. 6. Table 3 provides the values of $M\sigma_{sys}$ so obtained. The agreement between theoretical and experimental profiles in Fig. 6, which is generally very good, was optimized in terms of a single quantity: for nylon, the difference between the values of CT number at the peak and trough. In the case of Cu this quantity was the value of CT number at the peak. There was no convenient quantity in the case of Al, given the shape of the associated experimental profiles, and so the corresponding theoretical profiles in Fig. 6 are based on the averages of the optimum $M\sigma_{sys}$ values for nylon and Cu, at each X-ray energy. The theoretical Al profiles in Fig. 6 contain some, albeit small, indications of phase contrast which are not present in the experimental profiles (or are much less obvious). This may be a reflection of the Al wire 'surface quality' being poorer than we have modelled it to be, but is most likely a consequence of the geometrical effect discussed in §4.1 [which gives rise to the distinctly non-circular Al-wire cross-section in reconstructed (xz) slices].

The magnitude of the values of $M\sigma_{sys}$ in Table 3 are quite consistent with our detailed considerations above. It is particularly encouraging that the values obtained *independently* for nylon and Cu are reasonably consistent at each X-ray energy. Although we have not explicitly addressed the point thus far, it is of course quite possible for $M\sigma_{sys}$ to be energy dependent, and so we cannot necessarily expect the values to be in agreement from one X-ray energy to another. Bourgeois *et al.* (1994), for example, have used synchrotron radiation to measure the FWHM of the PSF for several X-ray imaging systems as a function of energy, the range encompassing the X-ray energies employed in the present study. Whilst the X-ray imaging systems studied are quite different from the
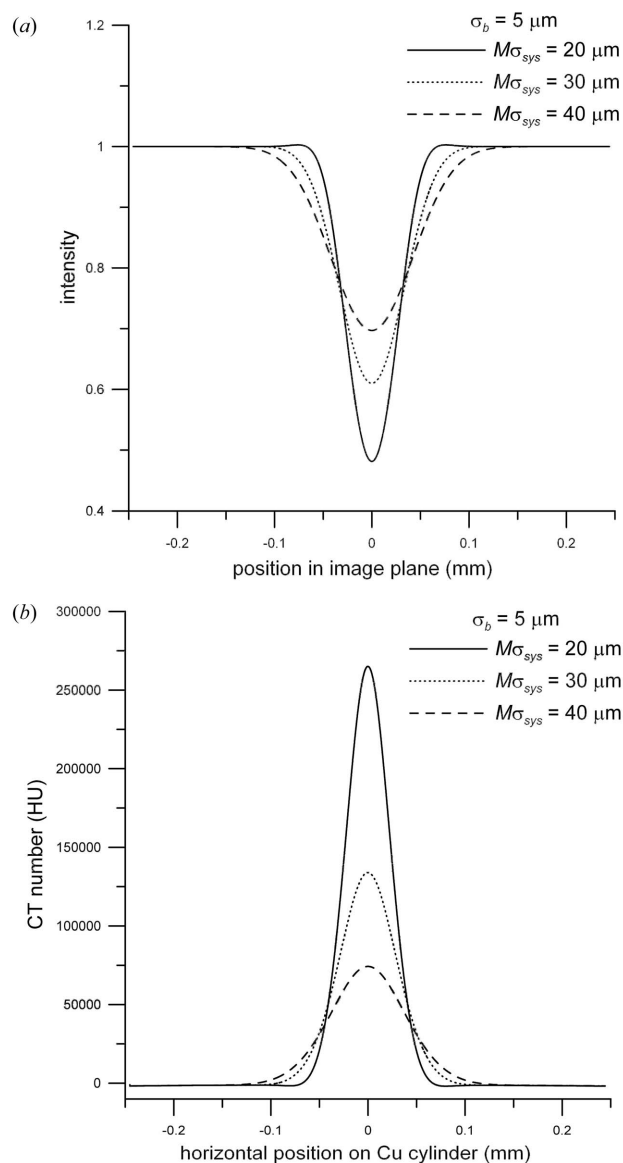

Figure 10
(*a*) Profiles from image simulations using the Fresnel–Kirchhoff formula for a 60 µm-diameter Cu cylinder and 25.52 keV X-rays. The curves correspond to different widths of the PSF. (*b*) CT-number profiles through a reconstructed *xz* slice from image simulations using the Fresnel–Kirchhoff formula for a 60 µm-diameter Cu cylinder and 25.52 keV X-rays. The curves correspond to different widths of the PSF. Further details are provided in the text.

CCD used here, the closest, an image intensifier/CCD with a Be window, has a PSF whose FWHM is almost constant with energy (there is in fact a very slight decrease with increasing energy). Whilst certainly not highly compelling evidence in favour of, this trend is at least consistent with, the results in Table 3.

We now have the situation where we can quite accurately account for all of the quantitative experimental X-ray tomography data. The remaining question relates to our acceptance of the relatively larger values of $M\sigma_{sys}$, especially for Cu, at 12.66 keV. In the event that this behaviour is deemed to be anomalous, we still need to account for this effect in terms of some additional, hitherto unidentified, energy-dependent phenomenon which predominates for Cu. A likely candidate would seem to be harmonic contamination and we will investigate this possibility in detail in the next subsection (§4.3). Tran *et al.* (2003), for example, in connection with accurate measurements of X-ray absorption coefficients using synchrotron data, have undertaken a quantitative determination of the effect of harmonic contamination. If we consider the case where we have a primary X-ray beam incident on the sample which is composed of 99% 12.66 keV photons (fundamental) and 1% 37.98 keV photons ($\lambda/3$ harmonic), then the transmitted beam would have: essentially the same composition after traversing 1.2 mm of nylon; only 86% fundamental, plus 14% $\lambda/3$ harmonic after traversing 0.83 mm of Al; just 19% fundamental, plus 81% $\lambda/3$ harmonic after traversing 60 µm Cu. This is, of course, a form of beam hardening and provides an indication of why harmonic contamination could manifest itself preferentially in the Cu results. The figures quoted correspond to the case of a perfect imaging system ($M\sigma_{sys} = 0$) and the impact of harmonic contamination will be considerably less dramatic when allowance is made for the real PSF (this will be demonstrated in §4.3). The fact that harmonic contamination is not expected to have any significant effect in the case of the nylon results, and that the value of $M\sigma_{sys}$ in Table 3 for nylon at 12.66 keV is larger than for the other X-ray energies, suggests that we are seeing a 'real' energy dependence in the PSF width. However, this cannot be stated categorically, and the value of $M\sigma_{sys}$ at 12.66 keV being slightly larger for Cu compared with nylon indicates that further investigation is justified.

In terms of the effects of harmonic contamination as a function of X-ray energy, a number of factors need to be considered, including the quantum efficiency and response of the CCD, *e.g.* the quantum efficiency will decrease from 72% at 12.66 keV to 11% at 30.49 keV; however, the presence of the Gd K-edge at 50.24 keV for the Gadox phosphor means that all harmonics (for example, the lowest-energy $\lambda/4$ harmonic at 50.64 keV) will then have a somewhat enhanced quantum efficiency except for the lowest-energy $\lambda/3$ harmonic (37.98 keV).

4.3. Contributions due to harmonic contamination

Fig. 11 displays the results of numerical image simulations for the 60 µm Cu cylinder and 12.66 keV (fundamental)
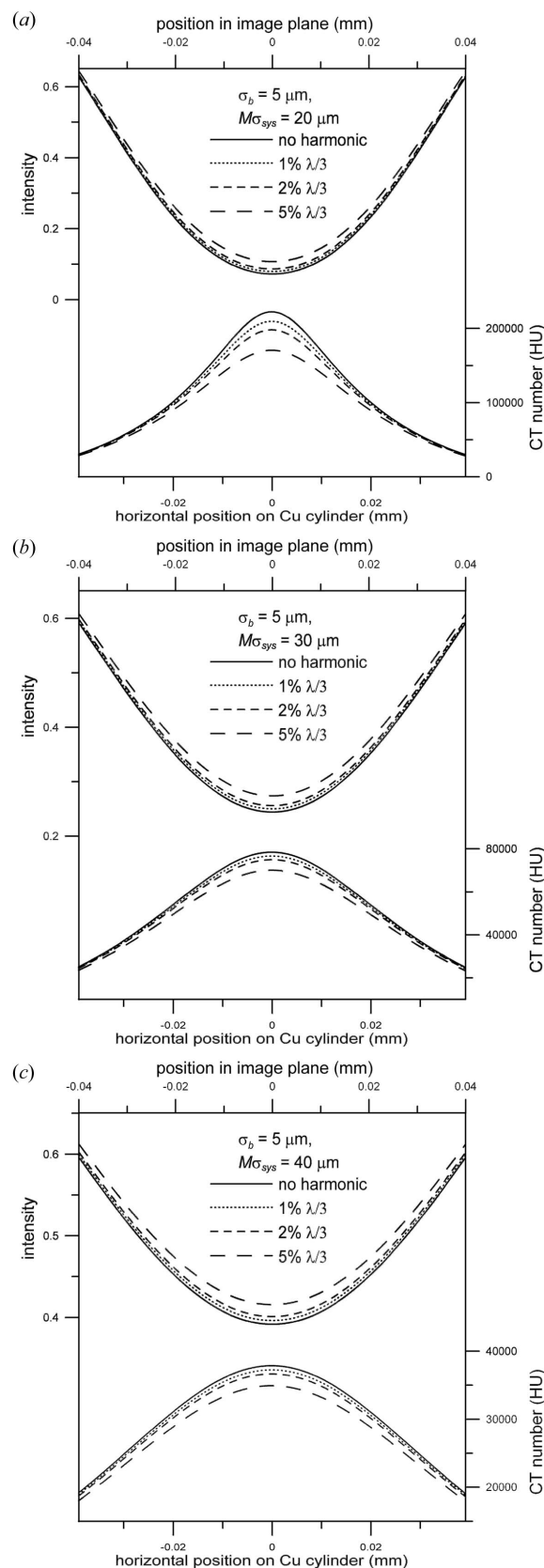

Figure 11
Intensity and CT-number profiles from image simulations using the Fresnel–Kirchhoff formula for a 60 µm-diameter Cu cylinder and 12.66 keV X-rays, allowing for different levels of harmonic ($\lambda/3$) contamination. The curves correspond to (*a*) $M\sigma_{sys} = 20$ µm; (*b*) $M\sigma_{sys} = 30$ µm; (*c*) $M\sigma_{sys} = 40$ µm. Further details are provided in the text.

X-rays, with different levels of harmonic ($\lambda/3$) contamination (0, 1, 2 and 5%). In Fig. 11(a) we have used $M\sigma_{sys} = 20$ µm, in Fig. 11(b) $M\sigma_{sys} = 30$ µm, and in Fig. 11(c) $M\sigma_{sys} = 40$ µm (all with $\sigma_b = 5$ µm). In each figure there are one-dimensional intensity profiles (top) through the simulated two-dimensional X-ray images, and the corresponding CT-number profiles (bottom) through a (central) reconstructed xz slice. The range covered in the image plane has been limited to 80 µm ($80/M = 78.3$ µm at the sample). As alluded to in §4.2, the effects of harmonic contamination are most significant for smaller values of $M\sigma_{sys}$.

We will now describe the detailed calculations we have performed in order to estimate the harmonic contamination contributions as accurately as possible. The angular flux density was calculated (ignoring, for the present, the presence of the monochromator) at the CCD (24 m) as a function of X-ray energy from 1 to 150 keV in steps of 0.1 keV using the program *SPECTRA 8.1* (Tanaka & Kitamura, 2001; http://radiant.harima.riken.go.jp/spectra/). The storage-ring parameter values for the Australian Synchrotron were taken from http://radiant.harima.riken.go.jp/spectra/asp.prm. The wiggler field was initially taken to be 0.838 T (see §2 for further details). Fig. 12 shows the resulting flux-density curve (solid). When allowance is made for all of the filters, windows and beam paths we get the dotted curve in Fig. 12. It is then necessary to make allowance for the quantum efficiency and response of the CCD. The former is accomplished by including the multiplicative factor $1 - \exp(-\mu_m\rho_s)$, where μ_m is the energy-dependent mass absorption coefficient. The CCD response takes account of the fact that the number of visible photons produced is not only directly proportional to the number of incident X-ray photons but also to their energy, *e.g.* the CCD detector signal associated with a single 60 keV X-ray photon is three times that for a single 20 keV X-ray photon.
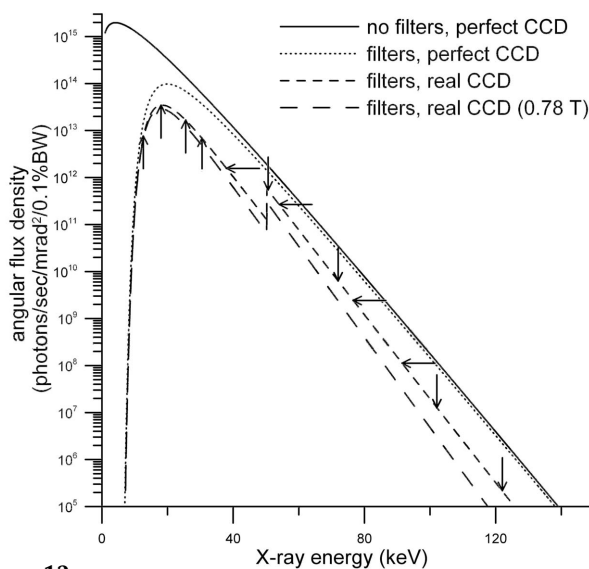

Figure 12
Angular-flux-density calculations, including the effects of filters, windows and beam paths, and the quantum efficiency and response of the CCD. One curve is for a wiggler field of 0.78 T, and the others for 0.838 T. The arrows indicate the position of the fundamental X-ray energies and harmonics. Further details are provided in the text.

The short-dashed curve in Fig. 12 shows the result of including the detector efficiency and response. The nature of the detector response results in this curve being on a relative, rather than an absolute, flux-density scale (we have scaled the curve so that the response at the peak is unity). Finally, the long-dashed curve in Fig. 12 is the same as the short-dashed curve except that the wiggler field is 0.78 T instead of 0.838 T (see §2 for further details). The vertical (up) arrows show the positions of the four (fundamental) X-ray energies used. The horizontal arrows correspond to the $\lambda/3$ harmonics, and the vertical (down) arrows to the $\lambda/4$ harmonics. The weighted-average X-ray energies for the curves in Fig. 12 are 9.6, 23.8, 21.7 and 21.1 keV, respectively.

In order to ascertain the peak reflectivity of the Si mono-lithic double-crystal monochromator for the fundamental X-ray energies and harmonics we use the perfect-crystal dynamical theory of X-ray diffraction. The two Si components are assumed to be perfectly flat, effectively infinite thickness, with sufficiently extended surfaces to intercept the entire X-ray beam, and with symmetric (111) surfaces. The dynamical-theory formulation is simplified by the fact that we only need to consider the normal (σ) component of polarization (polarization factor is unity), that Si possesses the centro-symmetric[12] diamond crystal structure, and that we will only be concerned with symmetric hhh Bragg reflections, *i.e.* those for which the Miller indices are all equal to integer h. If we neglect bonding effects and anharmonic thermal vibrations, it can be shown that the conventional X-ray structure factor is given by

$$F_h(\lambda) = \left[f_0(h) + f'(\lambda) + if''(\lambda) \right] T(h)\Gamma(h)$$
$$\equiv F'_h(\lambda) + iF''_h(\lambda), \qquad (19)$$

where $f_0(h)$ is the free-atom spherical scattering factor for Si, $f'(\lambda)$ and $f''(\lambda)$ are the anomalous dispersion corrections for Si, and $T(h)$ is the harmonic temperature factor for Si. $f_0(h)$ is also dependent on the Si lattice parameter (5.4309 Å; NBS, 1976) and we use the atomic scattering-factor parameterization of Doyle & Turner (1968). The values of the anomalous dispersion corrections were calculated with the aid of data from Brennan & Cowan (1992). $T(h)$ also depends on the lattice parameter and the Si Debye–Waller factor (0.45 Å^2; Prager, 1971). The value of $\Gamma(h)$ is 8 if $h \equiv 0 \pmod 8$, $-4\sqrt{2}$ if $h \equiv \pm 1 \pmod 8$, 0 if $h \equiv \pm 2 \pmod 8$, $4\sqrt{2}$ if $h \equiv \pm 3 \pmod 8$, and -8 if $h \equiv 4 \pmod 8$. We will not be directly concerned with the modulus of the structure factor here, but, for completeness,

$$\left| F_h(\lambda) \right| = \left\{ \left[f_0(h) + f'(\lambda) \right]^2 + \left[f''(\lambda) \right]^2 \right\}^{1/2} T(h) \left| \Gamma(h) \right|$$
$$\equiv \left\{ \left[F'_h(\lambda) \right]^2 + \left[F''_h(\lambda) \right]^2 \right\}^{1/2}. \qquad (20)$$

---

[12] The diamond structure (space group $Fd\bar{3}m$) is not centrosymmetric about the conventional unit-cell origin [where the eight atom positions are (0,0,0) plus the three equivalent face-centred cubic (f.c.c.) sites and (1/4, 1/4, 1/4) plus three f.c.c. sites]. However, there is a centre of symmetry at the mid-point of each nearest-neighbour bond, such as (1/8, 1/8, 1/8), and so we choose this position as the origin and have new atom positions of ±(1/8, 1/8, 1/8) plus f.c.c. sites instead.

Equation (20) shows that the Bragg reflections for which h is odd (*e.g.* 111 and 333) will in general be reasonably strong ($|\Gamma(h)| = 4\sqrt{2}$) and those for which h is even and an even multiple of two (*e.g.* 444 and 888) will in general be (relatively) stronger still ($|\Gamma(h)| = 8$). However, if h is even and an odd multiple of two (*e.g.* 222 and 666) the Bragg reflection is 'forbidden', remembering that we have explicitly neglected the small contributions due to bonding effects and anharmonic thermal vibrations in the present study [see, for example, the detailed (temperature-dependent) X-ray study of both effects performed by Roberto & Batterman (1970) in respect of the 222 reflection in Si].

The X-ray susceptibility (or polarizability) can then be expressed as

$$\chi_h(\lambda) = \chi'_h(\lambda) + i\chi''_h(\lambda), \tag{21a}$$

where

$$\chi'_h(\lambda) = -\frac{r_e \lambda^2}{\pi V} F'_h(\lambda) \tag{21b}$$

and

$$\chi''_h(\lambda) = -\frac{r_e \lambda^2}{\pi V} F''_h(\lambda), \tag{21c}$$

and r_e is the classical electron radius and V the unit-cell volume. For a non-centrosymmetric crystal structure $\chi'_h(\lambda)$ and $\chi''_h(\lambda)$ can themselves be complex, but for the present case of a centrosymmetric crystal structure these components are both real.

Using the dynamical-theory formalism of Cole & Stemple (1962) [see also Zachariasen (1945)] the reflectivity curve (reflecting power) is given by

$$R = L - (L^2 - 1)^{1/2}, \tag{22}$$

where

$$L = \frac{y^2 + g^2 + \left[(y^2 - g^2 - 1 + p^2)^2 + 4(gy - p)^2\right]^{1/2}}{1 + p^2}, \tag{23}$$

$$y = \frac{\chi'_0(\lambda) + (\theta - \theta_B)\sin 2\theta_B}{\chi'_h(\lambda)}, \tag{24}$$

$$g = \chi''_0(\lambda)/\chi'_h(\lambda) \tag{25}$$

and

$$p = \chi''_h(\lambda)/\chi'_h(\lambda), \tag{26}$$

with θ being the angle between the incident X-ray beam and the Bragg planes. Certain important quantities which result from the dynamical theory of X-ray diffraction include [see, for example, Matsushita & Hashizume (1983) and Authier (2001)], for the present study, the extinction distance

Table 4
Values of certain parameters and calculated quantities for relevant Bragg reflections and X-ray wavelengths.

Rows with the same typeface belong to the same group of fundamental/harmonics. Further details are provided in the text.

hhh	E (keV)	λ (Å)	θ_B (°)	Λ_h (μm)	ω_h (arcsec)	δθ_h (arcsec)	(Δλ/λ)_h
111	*12.66*	*0.9795*	*8.986*	*30.14*	*4.292*	*4.064*	*1.316 × 10⁻⁴*
111	*18.00*	*0.6889*	*6.307*	*43.34*	*2.985*	*2.824*	*1.309 × 10⁻⁴*
111	*25.52*	*0.4859*	*4.444*	*61.95*	*2.088*	*1.976*	*1.302 × 10⁻⁴*
111	30.49	0.4067	3.718	74.19	1.744	1.658	1.301 × 10⁻⁴
333	**37.98**	**0.3265**	**8.986**	**163.7**	**0.2634**	**0.4472**	**8.075 × 10⁻⁶**
333	**54.00**	**0.2296**	**6.307**	**235.0**	**0.1834**	**0.3126**	**8.046 × 10⁻⁶**
333	*76.56*	*0.1620*	*4.444*	*334.4*	*0.1290*	*0.2189*	*8.045 × 10⁻⁶*
333	91.47	0.1356	3.718	400.3	0.1077	0.1833	8.038 × 10⁻⁶
444	**50.64**	**0.2449**	**8.986**	**216.0**	**0.1497**	**0.2514**	**4.591 × 10⁻⁶**
444	**72.00**	**0.1722**	**6.307**	**311.2**	**0.1039**	**0.1757**	**4.557 × 10⁻⁶**
444	*102.1*	*0.1215*	*4.444*	*442.1*	*0.07316*	*0.1234*	*4.564 × 10⁻⁶*
444	122.0	0.1017	3.718	528.6	0.06120	0.1033	4.566 × 10⁻⁶
555	**63.30**	**0.1959**	**8.986**	**562.5**	**0.04599**	**0.1611**	**1.410 × 10⁻⁶**
777	**88.62**	**0.1399**	**8.986**	**1706**	**0.01083**	**0.08222**	**3.320 × 10⁻⁷**

$$\Lambda_h = \lambda \cos\theta_B / |\chi_h|, \tag{27}$$

the intrinsic or Darwin width of the Bragg reflection

$$\omega_h = 2|\chi'_h|/\sin 2\theta_B \tag{28}$$

and the deviation from the exact Bragg angle due to refraction effects

$$\delta\theta_h = -\chi'_0/\sin 2\theta_B. \tag{29}$$

It can easily be shown, using Bragg's Law, that the relative wavelength spread associated with the Darwin width is given by

$$\left(\frac{\Delta\lambda}{\lambda}\right)_h = -\left(\frac{\Delta E}{E}\right)_h = \omega_h \cot\theta_B = \frac{|\chi'_h|}{\sin^2\theta_B}. \tag{30}$$

Given that the X-ray wavelengths or energies considered in this study are well removed from the Si absorption edges it can be shown that, for a particular Bragg reflection, Λ_h varies as λ^{-1} to a good approximation, ω_h as λ, and $(\Delta\lambda/\lambda)_h$ remains constant [$\delta\theta_h$ also varies as λ for a particular Bragg reflection and, additionally, varies as λ^2 (or h^{-2}) for a series of harmonics (where θ_B is constant)]. Table 4 provides the calculated values of these quantities for the relevant Bragg reflections and X-ray wavelengths.

The IMBL front-end mask defines an X-ray beam of divergence 5.0 mrad horizontally and 0.3 mrad vertically. The water-cooled primary slits (hutch 1A), defining the beam in the horizontal and vertical directions, are at 13.7 m and 14.0 m from the source, respectively. The horizontal-defining slits had an opening of approximately 6 mm and the vertical-defining slits 1.0 mm (precisely determined). These slit sizes represent a quite significant aperturing of the primary X-ray beam, and were verified by exposures taken with Gafchromic film (HD-810; ISP Inc.) placed on the CCD (with the monochromator out of the primary beam). We are particularly concerned with the vertical-defining slit since this dictates the beam divergence ($\delta\theta_d$) in the plane of diffraction (vertical) for the monochromator (this slit subtends an angle of 0.071 mrad or

15 arcsec at the source). It is easily shown geometrically that a source of size s and a slit of size a, separated by a distance d_1, will produce a beam size at distance d_2 from the slit of $|M'(s \pm a) - s|$, where $M' = (d_1 + d_2)/d_1$ is the simple geometric magnification factor, and the upper sign is for the penumbra and the lower sign for the umbra. In the limiting case where $s \ll a$, the sizes of the umbra and penumbra are equal, with a value $M'a$. At the other limit, where $s \gg a$, they are also equal, but with a value $(M' - 1)s$.[13] In the present case, and taking s to have the (σ-) values mentioned in §4.2, the sizes of X-ray beam umbra and penumbra at the CCD differ by only 1.3% in the vertical direction, and by 4.9% in the horizontal direction. The corresponding figures when we use FWHM values for s are 3.2% and 11.7%, respectively. This is consistent with the quite anisotropic nature of the source having a significant impact on the X-ray beam profile, and the effects are clearly visible when the sharpness of the horizontal and vertical edges of the Gafchromic-film exposures are compared.

We have used *SPECTRA 8.1* to calculate profiles of the angular flux density at the CCD (24 m; without monochromator) as a function of vertical and horizontal position, about the centre of the X-ray beam (wiggler field 0.838 T). These calculations have been performed for all the X-ray energies of concern, including harmonics, with vertical and horizontal step sizes of 100 µm and 1 mm, respectively. The results for an X-ray energy of 12.66 keV, and all its harmonics up to $\lambda/7$, are shown in Figs. 13(*a*) and 13(*b*) (horizontal and vertical positions, respectively), the profiles having been normalized for ease of presentation; the absolute angular-flux-density values at 0 mm are those plotted in the uppermost curve of Fig. 12. The limits of the X-ray beam, as defined by the primary slits, are shown as vertical lines for both the umbra (solid lines) and penumbra (dashed lines); their calculated positions are based on FWHM-values for s. The increase of 'roll-off' of the angular flux density with increasing X-ray energy is quite apparent, especially in the vertical direction, and we will make allowance for this effect in our calculations of harmonic contamination (see below).

The differential form of Bragg's law $[(\Delta\lambda/\lambda) = \Delta\theta \cot\theta_B$; used to obtain (30)] yields a maximum value of $\Delta\lambda$ corresponding to the beam divergence associated with the X-ray beam represented in Fig. 13(*b*), of $(\Delta\lambda)_d = 0.45$ mÅ for the Bragg reflections in Table 4. This value is significantly larger than any of the values associated with the Darwin width, $(\Delta\lambda)_h = \lambda(\Delta\lambda/\lambda)_h$, obtained from Table 4, which lie in the range from essentially zero up to 0.13 mÅ. That is, the wavelength spread associated with the divergence of the primary X-ray beam will in general dominate over that associated with the Darwin width for the monochromator Bragg

---

[13] Similarly, the beam divergence can be shown to be $|s \pm a|/d_1$, which has the values, equal for both umbra and penumbra, of a/d_1 and s/d_1 for the limiting cases of $s \ll a$ and $s \gg a$, respectively. In the present case, $s < a$, both horizontally and vertically, and we have calculated the beam divergence to be the angle subtended by the penumbral beam at the true (not the effective, point) source position, a value which lies in between the values obtained when considering umbral and penumbral beam sizes in conjunction with their respective effective point-source positions.
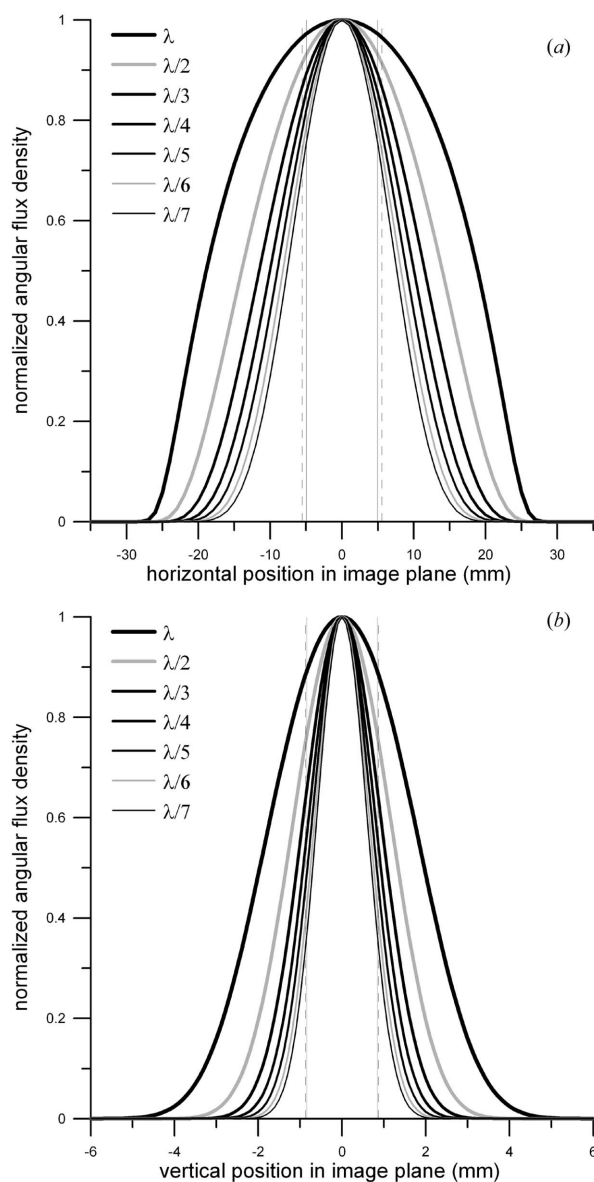

Figure 13
(Normalized) angular-flux-density calculations for a wiggler field of 0.838 T and a (fundamental) X-ray energy of 12.66 keV plus harmonics in the (*a*) horizontal direction, (*b*) vertical direction. The vertical lines mark the edges of the X-ray beam as defined by the primary slits (solid lines for umbra and dashed lines for penumbra). The $\lambda/2$ and $\lambda/6$ harmonics are shown in grey because they relate to 'forbidden' Bragg reflections (222 and 666, respectively). Further details are provided in the text.

reflections we are considering here. A convenient way of considering these issues is *via* the use of DuMond diagrams (DuMond, 1937). The DuMond diagram provides a versatile and intuitive graphical approach to understanding the correlations imposed by X-ray optical elements, such as slits and monochromators, in angle–wavelength (θ–λ) space. In the case of a double-crystal monochromator one normally needs to consider a separate DuMond diagram for each crystal. However, in the present case of a monolithic (+, −) monochromator which has two rigidly linked crystal elements with parallel sets of Bragg planes (the so-called 'non-dispersive
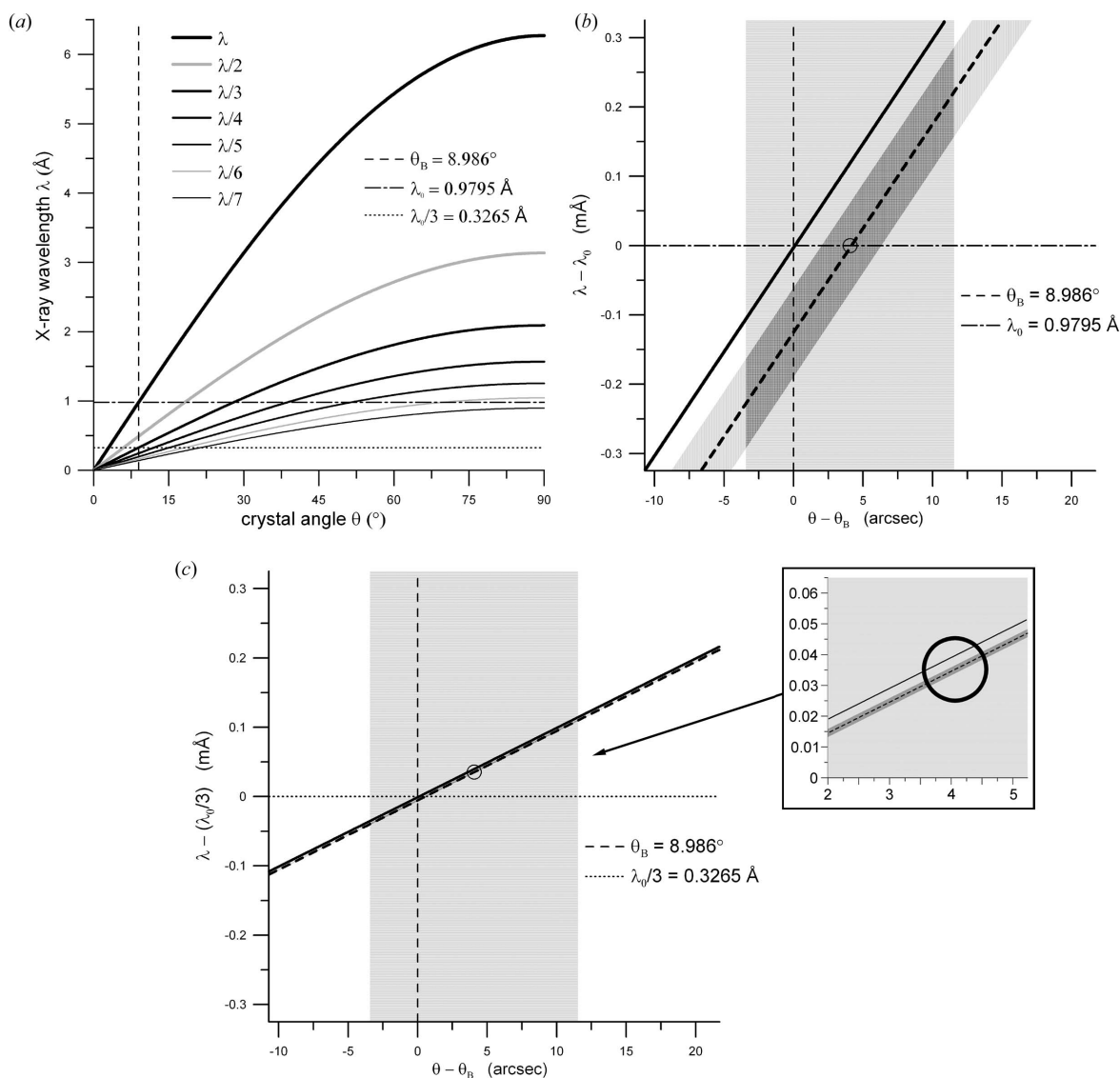
Figure 14
DuMond diagrams corresponding to the 12.66 keV case. (*a*) The full DuMond diagram and including harmonics up to $\lambda/7$. (*b*) Magnified (by a factor of 10^4) version in the vicinity of the fundamental (λ). (*c*) Magnified (by a factor of 10^4) version in the vicinity of the $\lambda/3$ harmonic. The effects of the Darwin width and the beam divergence are incorporated and the intersection of the associated lightly shaded regions, represented by the darkly shaded parallelogram, will be the focus of our attention. The effect of refraction is also included in the diagrams. In (*a*) the $\lambda/2$ and $\lambda/6$ harmonics are shown in grey because they relate to 'forbidden' Bragg reflections (222 and 666, respectively). In (*c*) we have included an insert graph with an enlarged view for clarity. Further details are provided in the text.

parallel configuration'), these two DuMond diagrams exactly overlap and we need consider just one.[14]

Fig. 14(*a*) shows the full DuMond diagram corresponding to the 12.66 keV case, and including harmonics up to $\lambda/7$. Figs. 14(*b*) and 14(*c*) show magnified (by a factor of 10^4)

[14] This statement should not, however, be taken to mean that the reflectivity curves for a single such crystal and for the double-crystal monochromator are the same. As a simple example we can consider two points on the single-crystal reflectivity curve for a single X-ray wavelength and a single beam divergence angle. One point is on the peak and has a value of 0.9, and one is on a tail and has a value of 0.1. The reflectivity values for the corresponding double-crystal monochromator we are considering in the present study would have values of $(0.9)^2 = 0.81$ and $(0.1)^2 = 0.01$, respectively. This simple example also serves to demonstrate the well known effect, first demonstrated by Bonse & Hart (1965), of using multiple Bragg reflections in a channel-cut monochromator to preferentially reduce the tails, *i.e.* compare 0.9/0.1 = 9 with 0.81/0.01 = 81.

versions of the DuMond diagram in the vicinity of the fundamental (λ) and $\lambda/3$ harmonic, respectively. In such small regions of θ–λ space, the differential form of Bragg's law can be applied directly and the curve treated as a straight line of gradient $\lambda \cot \theta_B$. The effect of refraction is to move this line by an amount $\delta\theta_h$ [see (29)] parallel to the horizontal (θ) axis; see the dashed lines, parallel to and displaced from the original lines. The lightly shaded region about the dashed line, in each case, has a width, parallel to θ, of ω_h [see (28)], corresponding to the extent of the effect associated with the Darwin width. The lightly shaded region with sides parallel to both the θ and λ axes corresponds to the effect of the X-ray beam divergence and has a width of $\delta\theta_d$. Both of these lightly shaded regions have effectively infinite extent in the λ direction, but our concern will be with the region where the two intersect,

represented by the darkly shaded parallelogram. In the case of Fig. 14(c), the values of $\delta\theta_h$ and ω_h are quite small compared with $\delta\theta_d$ and so we have included an insert graph with an enlarged view for clarity. Important properties of this parallelogram, for a particular fundamental and associated harmonics, are as follows:

(i) Area:

$$\delta\theta_d \omega_h(\lambda_0/n)\lambda_0 \cot\theta_B/n; \qquad (31a)$$

(ii) Abscissa of centre:

$$\theta - \theta_B = \delta\theta_h(\lambda_0); \qquad (31b)$$

(iii) Ordinate of centre:

$$\lambda - (\lambda_0/n) = \lambda_0 \cot\theta_B\big[\delta\theta_h(\lambda_0) - \delta\theta_h(\lambda_0/n)\big]/n$$
$$\simeq \frac{4\lambda_0^3 Z r_e}{\pi V \sin^2\theta_B}\frac{1}{n}\left(1 - \frac{1}{n^2}\right), \qquad (31c)$$

where n denotes the number of the harmonic [for the fundamental $n = 1$, and the ordinate corresponds to $\lambda = \lambda_0$ as expected; see Fig. 14(b)]. The approximate expression in (31c) is obtained by replacing, for Si, $F_0'(\lambda)$ by $8Z$ [see (19) and (21b)], where Z is the atomic number (14 for Si), i.e. we are neglecting the real anomalous dispersion correction $f'(\lambda)$. The centre of the parallelogram, given by (31b) and (31c), is marked by a small circle in Figs. 14(b) and 14(c) and it is apparent that, whilst $\lambda_0/3 = 0.3265$ Å is within the range of those wavelengths which make a contribution, it is not actually at the centre of this wavelength band (which is [0.32646, 0.32661] Å). This is a consequence of the fact that the size of the deviation from the exact Bragg angle due to refraction effects is different for the fundamental and its harmonics. The centre of the parallelogram for the fundamental is determined by the fact that we initially calibrated our λ_0 values with reference to the K-edges of certain filters (see §2).

We have performed extensive dynamical-theory calculations for each of the cases given in Table 4 using (19) and (21a)–(26), for the monolithic double-crystal monochromator. The results of individual reflectivity-curve calculations for values of θ and λ covering a particular DuMond-diagram parallelogram are combined to yield the final results. Whilst the θ values sampled must fall within the range dictated by the divergence of the X-ray beam, we can choose (for convenience) to map the full rectangle, with vertical and horizontal sides, which bounds the parallelogram, without compromising the calculation results. However, the area of this rectangle is $(\omega_h + \delta\theta_d)/\omega_h$ times larger than that of the parallelogram and whilst this factor is less than 5 for the 12.66 keV fundamental it will exceed 10^3 for the corresponding $\lambda/7$ harmonic (see Table 4 for the ω_h values). Thus, in the interests of avoiding issues of undersampling or lengthy computation times, we have ensured that our computer program has the flexibility to map a parallelogram in θ–λ space. In the interests of being conservative, and allowing for the fact that individual reflectivity curves have tails extending beyond the angular range associated with the Darwin width, we have considered parallelograms which are twice the prescribed 'thickness' in λ, i.e.

$2(\Delta\lambda)_h$ [resulting in an overall range in λ for the parallelogram of $(\Delta\lambda)_d + 2(\Delta\lambda)_h$]. Individual reflectivity-curve calculations were performed for a regular grid of (θ, λ) points covering each parallelogram, with 101 equally spaced points along each line parallel to the θ axis, and the same along each line parallel to the λ axis. The number of such calculations varied from approximately 1.8×10^4 (for the 12.66 keV case) to approximately 6.9×10^6 (for the 88.62 keV case). The variation of angular flux density with X-ray wavelength within the DuMond diagrams being considered here amounts to a less-than-1% effect in all cases, and so we have used top-hat distributions as a function of λ. However, in order to allow for the roll-off of the angular flux density as a function of θ in the vertical direction we have included a θ-dependent weighting factor at each point. The value of this weighting factor was obtained by performing least-squares fits to curves such as those shown in Fig. 13(b) for each X-ray energy. Whilst the overall shape of these curves is not Gaussian, we found that we could obtain excellent Gaussian fits within the vertical divergence range of concern here, i.e. between the vertical dashed lines in Fig. 13(b), calculated to span 14.96 arcsec. The third column in Table 5 lists the values of the refined parameter, the FWHM of the Gaussian [the peak height for the Gaussian fit to the (normalized) angular-flux-density curve was also refined, but the value obtained was always unity].

In the approach which we have adopted here it is implicit that we are treating the double-crystal monochromator as an X-ray optical element which does not itself alter the spatial distribution of the beam which illuminates the sample (apart from the obvious displacement vertically) but rather acts like a special 'filter'. We have not concerned ourselves with correlations, at the sample position, between wavelength, direction of propagation and x–y position for the incident X-rays. This is quite justifiable for the imaging/tomographic study being reported here; however, if the X-ray beam after the monochromator was being used for certain diffraction-based experiments for example, a more detailed approach may need to be considered. The DuMond-diagram approach adopted here can be extended [see, for example, Xu & Li (1988) and Servidori et al. (2001)], alternatively the phase-space method can be used [see, for example, Hastings (1977) and Pianetta & Lindau (1977)], or a combination of both can be applied [see, for example, Matsushita et al. (1978) and Matsushita & Kaminaga (1980)]. It should also be pointed out that we will not attempt to allow for the variation of harmonic contamination from point to point across the monochromated X-ray beam, although results such as those presented in Fig. 13 could form the basis for such an undertaking. This variation is, however, accounted for in an average sense, in our consideration of the tomographic data sets.

The dynamical-theory calculations yield a factor, shown in the fourth column of Table 5, which, when multiplied by the angular flux density from Fig. 12, will provide us with the value of the integrated flux in the 'monochromatic' beam for the associated X-ray energy. Before applying this factor we need to allow for the roll-off of the angular flux density with θ in the horizontal direction. As shown in Fig. 13(a), this effect is not

Table 5
Results of dynamical-theory calculations, made in connection with estimating the extent of harmonic contamination, for relevant Bragg reflections and X-ray wavelengths.

It should be noted that the values of integrated flux in the last two columns are on a relative rather than an absolute scale (the percentage values in brackets are absolute) due to the allowance for the CCD response. Rows with the same typeface belong to the same group of fundamental/harmonics. Further details are provided in the text.

					Integrated flux (photons s^{-1})			
hhh	E (keV)	Gaussian FWHM (arcsec)	Dynamical-theory factor (mrad^2 0.1% bandwidth)	R_{horiz}	No filters Perfect CCD (0.838 T)	Filters Perfect CCD (0.838 T)	Filters Real CCD (0.838 T)	Filters Real CCD (0.78 T)
111	*12.66*	*35.78*	*4.099 × 10^{-3}*	*0.9884*	*3.85 × 10^{12} (99.9%)*	*6.12 × 10^{10} (95.5%)*	*3.01 × 10^{10} (98.6%)*	*2.71 × 10^{10} (99.1%)*
111	*18.00*	*28.59*	*4.192 × 10^{-3}*	*0.9813*	*1.86 × 10^{12}*	*3.74 × 10^{11}*	*1.42 × 10^{11}*	*1.18 × 10^{11}*
111	*25.52*	*23.24*	*4.142 × 10^{-3}*	*0.9710*	*5.59 × 10^{11}*	*2.75 × 10^{11}*	*6.68 × 10^{10}*	*4.99 × 10^{10}*
111	30.49	21.01	4.092 × 10^{-3}	0.9645	2.40 × 10^{11}	1.44 × 10^{11}	2.71 × 10^{10}	1.87 × 10^{10}
333	*37.98*	*18.60*	*2.455 × 10^{-4}*	*0.9546*	*3.96 × 10^{9} (0.1%)*	*2.70 × 10^{9} (4.2%)*	*3.68 × 10^{8} (1.2%)*	*2.27 × 10^{8} (0.8%)*
333	*54.00*	*15.44*	*2.336 × 10^{-4}*	*0.9344*	*2.10 × 10^{8}*	*1.59 × 10^{8}*	*5.83 × 10^{7}*	*2.84 × 10^{7}*
333	*76.56*	*12.94*	*2.179 × 10^{-4}*	*0.9075*	*2.93 × 10^{6}*	*2.33 × 10^{6}*	*4.84 × 10^{5}*	*1.69 × 10^{5}*
333	91.47	11.85	2.084 × 10^{-4}	0.8904	1.66 × 10^{5}	1.35 × 10^{5}	2.10 × 10^{4}	5.83 × 10^{3}
444	*50.64*	*15.97*	*1.343 × 10^{-4}*	*0.9384*	*2.23 × 10^{8}*	*1.68 × 10^{8} (0.3%)*	*6.75 × 10^{7} (0.2%)*	*3.47 × 10^{7} (0.1%)*
444	*72.00*	*13.34*	*1.253 × 10^{-4}*	*0.9128*	*3.98 × 10^{6}*	*3.15 × 10^{6}*	*7.23 × 10^{5}*	*2.70 × 10^{5}*
444	102.1	11.24	1.147 × 10^{-4}	0.8787	1.20 × 10^{4}	9.83 × 10^{3}	1.27 × 10^{3}	3.03 × 10^{2}
444	122.0	10.32	1.091 × 10^{-4}	0.8579	2.50 × 10^{2}	2.06 × 10^{2}	1.99 × 10^{1}	3.55 × 10^{0}
555	*63.30*	*14.24*	*3.940 × 10^{-5}*	*0.9228*	*6.36 × 10^{6}*	*4.94 × 10^{6}*	*1.40 × 10^{6}*	*5.96 × 10^{5}*
777	*88.62*	*12.03*	*8.587 × 10^{-6}*	*0.8936*	*1.17 × 10^{4}*	*9.51 × 10^{3}*	*1.55 × 10^{3}*	*4.53 × 10^{2}*

especially large in the present context and a relatively crude correction factor is sufficient. To this end we have performed Gaussian least-squares fits to the (normalized) angular-flux-density curves in the same manner as for the vertical direction. An expression for the correction factor (R_{horiz}) can then be obtained by deriving the average (ordinate-)value of the Gaussian within the region corresponding to the horizontal beam divergence (calculated to be 95.60 arcsec),

$$R_{horiz} = \frac{\pi^{1/2}}{2(\ln 2)^{1/2}\kappa} \, \text{erf}\left[(\ln 2)^{1/2}\kappa\right], \qquad (32)$$

where erf is the conventional error function and κ is the (dimensionless) ratio of the beam divergence to the refined FWHM-value from the Gaussian fit to the angular-flux-density curve. The values of R_{horiz} are provided in the fifth column of Table 5. The last four columns in Table 5 provide the resulting integrated flux values corresponding to each of the curves presented in Fig. 12. In those cases where the integrated flux for the fundamental is not 100.0% of the group of fundamental/harmonics, we have indicated the actual percentage in brackets, and, correspondingly, the values for the associated harmonics when they are not 0.0%. It is clear that the 12.66 keV fundamental is the only one for which harmonic contamination is of any significance. If there were no filters present and we had a perfect CCD, we predict just 0.1% of $\lambda/3$, as the fundamental and all harmonics are on the high-energy side of the peak in the angular-flux-density curve in Fig. 12. Once the X-ray beam is hardened as a result of the presence of the filters, the 12.66 keV fundamental and its $\lambda/3$ harmonic lie on opposite sides of the peak in the corresponding angular-flux-density curve in Fig. 12 and the $\lambda/3$ amounts to 4.2%, with the $\lambda/4$ being 0.3% (helped by the 444 being a strong Bragg reflection). In this case, where we have allowed for the filtration of the X-ray beam, the 18.00 keV fundamental is

very nearly at the peak of the angular-flux-density curve. When we allow for the energy-dependent efficiency of the CCD, the *apparent* extent of the harmonic contamination is reduced. However, this effect is offset to some extent by the energy-dependent response of the CCD, as discussed at the beginning of this subsection. This results in a 1.2% $\lambda/3$ contribution and a 0.2% $\lambda/4$ contribution; the latter, whilst being small, has been enhanced somewhat as a result of the X-ray energy being optimum with respect to the jump in the CCD efficiency which results from the presence of the Gd K-edge [see the previous subsection (§4.2)]. Finally, as discussed in §2, there is a possibility that the actual magnetic field in the insertion device is somewhat lower than the nominal value for an APS type A wiggler and the last column in Table 5 corresponds to this case. Whilst the exact value of the wiggler field, for a gap of 25 mm, is an important factor, it is clear that we are dealing with an apparent $\lambda/3$ component of approximately 1%. It should be emphasized that the extent of the harmonic contamination in the X-ray beam from the double-crystal monochromator is predicted to be significantly larger (see the third last column in Table 5), but the harmonic contamination as seen by the CCD is lower. In interpreting our experimental tomography data, inclusion of the performance of the CCD as a function of X-ray energy is an important factor when discussing harmonic contamination.

In summary, we have shown that there will indeed be a significant presence of harmonic contamination in the X-ray beam which is incident on the sample, but only for the lowest (fundamental) X-ray energy used (12.66 keV). This is exactly the type of effect we alluded to at the end of the previous subsection (§4.2). However, it is apparent from Fig. 11 [Fig. 11(*c*) in particular] that the magnitude of the effect associated with 1% harmonic contamination, for Cu, is still quite small. Thus the value of $M\sigma_{sys}$ = 50 µm, for Cu and 12.66 keV, in Table 3 would not be expected to decrease significantly as a result of

allowance for 1% harmonic contamination, *i.e.* we do not believe that this value of $M\sigma_{sys}$ was artificially increased to any significant extent in order to compensate for the unacknowledged presence of a $\lambda/3$ component. We thus conclude that the slightly higher values of $M\sigma_{sys}$ at 12.66 keV in Table 3 reflect an underlying dependence of the PSF on X-ray energy.

5. Discussion and conclusions

It is clear from the results we have obtained in §4 that the accurate characterization of the system PSF is crucial for any highly quantitative studies. The optimization of this PSF (for example, *via* the selection and operation of the X-ray imaging detector, or the choice of the wiggler gap and thereby the magnetic field which prevails in the insertion device) will be a key factor in the success of future experiments. There will of course always be some remaining (unwanted) contributions impacting adversely on the PSF, associated with the practicalities and limitations of any hardware or software involved in such experiments.

An obvious aspect of the present study which we have not addressed as yet is the possibility of deconvoluting the PSF we have established, from the X-ray images collected, prior to the tomographic reconstruction. Our ability to account, quantitatively, for the experimental results reported has relied, in part, on the use of computer simulations which have incorporated different theoretical PSFs through the procedure of convolution. This valuable opportunity has been afforded us by virtue of dealing with a well characterized phantom as the sample. In the case of a 'real-world' sample which we might wish to characterize, the possibility of being able to deconvolute the, independently determined, PSF from the experimental data is a very attractive one. Unfortunately, and unlike convolution, the inverse problem of deconvolution is in general mathematically 'ill-posed'. A detailed consideration of this 'ill-posedness' is beyond the scope of the present study and there is a wealth of literature on the subject [see, for example, Tikhonov & Arsenin (1977)]. In fact, as an operation, deconvolution does not have a direct definition in rigorous mathematical terms, but rather is defined as the inverse of the operation of convolution. In the present context it suffices to say that the solution of a given deconvolution problem may not exist, or may not be unique. A solution may also be quite unstable with respect to noise in the experimental data or quite sensitive to the precise description of the PSF.

In the present study, noise makes a significant contribution to the experimental X-ray images, and we also have the situation of the width of the PSF being comparable in size with certain key sample features (especially the Cu wire). Graafsma & de Vries (1999), for example, have demonstrated the utility of the maximum-entropy method for the deconvolution of PSFs from experimental X-ray images and Laue diffraction patterns. We have investigated both the Richardson–Lucy algorithm (Richardson, 1972; Lucy, 1974) and regularized Wiener deconvolution [see Wiener (1949)], as implemented in the *X-TRACT* software, and will report

Table 6
Experimental values of CT number in HU for the Cu component of the sample and each of the X-ray energies.

Theoretical values from Table 1 are also included for convenience. Further details are provided in the text.

	12.66 keV	18.00 keV	25.52 keV	30.49 keV
Parallel-beam reconstruction	294000 (24000)	338000 (7000)	202000 (4000)	196000 (4000)
Cone-beam reconstruction	307000 (16000)	347000 (5000)	212000 (3000)	201000 (8000)
Theory	395000	390000	311000	252000

briefly on results of the latter here. As indicated earlier we do not expect the CT-number values already reported for nylon and Al (see Table 1) to change as a result of considerations of the role of the PSF. Table 6 provides the experimental values of CT number for the Cu component at each of the four X-ray energies, resulting from the application of regularized Wiener deconvolution to the pre-processed images prior to tomographic reconstruction. We used the Gaussian PSFs as specified by the values of $M\sigma_{sys}$ given in italics in Table 3, and assumed the average signal-to-noise ratio to be 100. As expected, this deconvolution step did result in the presence of quite pronounced artefacts in the resulting X-ray images. These were clearly evident in the reconstructed slices and in fact such effects were exacerbated by the fact that, with the Cu component now demonstrating something approaching the true degree of absorption, the starburst artefacts mentioned in §4 have become quite prominent. In performing these tomographic reconstructions we tried a number of different filters (for example, Hamming, Hann, cosine, Shepp–Logan) with a view to reducing the impact of these artefacts, but there was no definitive improvement and the results reported here are for the (default) linear-ramp filter (which we have used previously). The experimental CT-number values in Table 6 represent the averages of the maximum values for the five central reconstructed (xz) slices in each case and can thus be compared most directly with the grey 'plus' symbols in Fig. 5. The σ's given in brackets in Table 6 are thus 'inter-slice' errors in the terminology we adopted in §3. We have included CT-number values based on both parallel-beam and cone-beam reconstructions in light of the results obtained earlier for simulations [see §4.2, and the insert graph in Fig. 9(b) in particular].[15] Whilst these experimental CT-number values are still smaller than the theoretical values, the discrepancies are greatly reduced (note that the factor by which the experimental value for 12.66 keV has increased is well over an order of magnitude). Given the issues associated with the deconvolution of the PSF from the X-ray images, these results are most encouraging.

In this paper we have performed a detailed analysis of the first monochromatic X-ray tomography data collected at IMBL, Australian Synchrotron. In order to account quan-

---

[15] The CT-number values for nylon and Al also increase, by approximately 3%, when cone-beam rather than parallel-beam reconstructions are performed. This does not change the excellent agreement between theory and experiment seen in Table 1 nor alter any of the discussion or conclusions.

titatively for the experimental results obtained for a simple three-component phantom at four different X-ray energies, we have considered in detail the role of harmonic contamination, phase-contrast effects and the system PSF. All three of these aspects have been shown to be significant, but it is the way in which the PSF affects the derived values of CT number, for the Cu component in particular, which is most relevant and pronounced. This Cu wire is the most highly absorbing of the three components and its diameter of just 60 µm is comparable in size with the width of the system PSF.

The use of a phantom which comprises simple features of known dimensions and material properties has enabled us to gain considerable insights into the capabilities and performance of the key beamline components such as the wiggler-based X-ray source itself, the double-crystal monochromator and the CCD detector. Such knowledge is of crucial importance to any quantitative analysis and interpretation of X-ray imaging/tomography data collected in the future for more complex samples consisting of unknown or poorly characterized materials. Such applications will occur in a variety of areas from materials science to the life sciences, with particular emphasis on medical and biomedical studies. Some aspects of the present investigations also have the potential to inform the conduct of and results obtained from other experiments performed at IMBL and other X-ray facilities, *e.g.* the need to accurately characterize the primary X-ray beam used for planned radiotherapy studies.

References

Abramowitz, M. & Stegun, I. A. (1965). *Handbook of Mathematical Functions with Formulas, Graphs and Mathematical Tables*, 1st ed. New York: Dover.
Albert, M., Naeser, M. A., Levine, H. L. & Garvey, A. J. (1984). *Arch. Neurol.* **41**, 1264–1269.
Authier, A. (2001). *Dynamical Theory of X-ray Diffraction, IUCr Monographs on Crystallography*, No. 11, 1st ed. Oxford University Press.
Barrett, J. F. & Keat, N. (2004). *Radiography*, **24**, 1679–1691.
Beltran, M. A., Paganin, D. M., Uesugi, K. & Kitchen, M. J. (2010). *Opt. Express*, **18**, 6423–6436.
Bonse, U. & Hart, M. (1965). *Appl. Phys. Lett.* **7**, 238–240.
Bourgeois, D., Moy, J. P., Svensson, S. O. & Kvick, Å. (1994). *J. Appl. Cryst.* **27**, 868–877.
Brennan, S. & Cowan, P. L. (1992). *Rev. Sci. Instrum.* **63**, 850–853.
Bronnikov, A. V. (2002). *J. Opt. Soc. Am. A*, **19**, 472–480.
Cole, H. & Stemple, N. R. (1962). *J. Appl. Phys.* **33**, 2227–2233.
Cormack, A. M. (1964). *J. Appl. Phys.* **34**, 2722–2727.
Cosslett, V. E. & Nixon, W. C. (1953). *J. Appl. Phys.* **24**, 616–623.
Cowley, J. M. (1975). *Diffraction Physics*, 1st ed. Amsterdam: North-Holland.
Donati, J.-F., Morin, J., Petit, P., Delfosse, X., Forveille, T., Aurière, M., Cabanac, R., Dintrans, B., Fares, R., Gastine, T., Jardine, M. M., Lignières, F., Paletou, F., Ramirez Velez, J. C. & Théado, S. (2008). *Mon. Not. R. Astron. Soc.* **390**, 545–560.
Donnelly, E. F., Price, R. R., Lewis, K. G. & Pickens, D. R. (2007). *Med. Phys.* **34**, 3165–3168.
Doyle, P. A. & Turner, P. S. (1968). *Acta Cryst.* A**24**, 390–397.
DuMond, J. W. M. (1937). *Phys. Rev.* **52**, 872–883.
Feldkamp, L. A., Davis, L. C. & Kress, J. W. (1984). *J. Opt. Soc. Am. A*, **1**, 612–619.
Galigekere, R. R., Wiesent, K. & Holdsworth, D. W. (1999). *Med. Phys.* **26**, 896–904.
Gaskill, J. D. (1978). *Linear Systems, Fourier Transforms and Optics*. New York: Wiley.
Gibbs, J. W. (1898). *Nature (London)*, **59**, 200.
Gibbs, J. W. (1899). *Nature (London)*, **59**, 606.
Glover, G. H. & Pelc, N. J. (1980). *Med. Phys.* **7**, 238–248.
Glover, G. H. & Pelc, N. J. (1981). *Med. Phys.* **8**, 799–807.
Golding, S. J. & Shrimpton, P. C. (2002). *Br. J. Radiol.* **75**, 1–4.
Graafsma, H. & de Vries, R. Y. (1999). *J. Appl. Cryst.* **32**, 683–691.
Graafsma, H. & Martin, T. (2008). In *Advanced Tomographic Methods in Materials Research and Engineering*, ch. 10, 1st ed., edited by J. Banhart. Oxford University Press.
Gradshteyn, I. S. & Ryzhik, I. M. (1965). *Table of Integrals, Series and Products*. New York: Academic Press.
Gross, F. B. (1995). *IEEE Trans. Antennas Propag.* **43**, 904–907.
Guigay, J. P. (1977). *Optik*, **49**, 121–125.
Guigay, J. P., Wade, R. H. & Delpla, C. (1971). *Electron Microscopy and Analysis*, edited by W. C. Nixon, pp. 238–239. London: Institute of Physics.
Gureyev, T. E., Nesterets, Ya. I., Stevenson, A. W., Miller, P. R., Pogany, A. & Wilkins, S. W. (2008). *Opt. Express*, **16**, 3223–3241.
Gureyev, T. E., Paganin, D. M., Myers, G. R., Nesterets, Ya. I. & Wilkins, S. W. (2006). *Appl. Phys. Lett.* **89**, 034102.
Hall Jr, M. M., Veeraraghavan, V. G., Rubin, H. & Winchell, P. G. (1977). *J. Appl. Cryst.* **10**, 66–68.
Hastings, J. B. (1977). *J. Appl. Phys.* **48**, 1576–1584.
Hegerl, R. & Hoppe, W. (1976). *Z. Naturforsch. Teil A*, **31**, 1717–1721.
Hounsfield, G. N. (1973). *Br. J. Radiol.* **46**, 1016–1022.
Hsieh, J. (2009). *Computed Tomography: Principles, Design, Artifacts, and Recent Advances*, 2nd ed. Washington: SPIE/John Wiley and Sons.
Hsieh, J., Molthen, R. C., Dawson, C. A. & Johnson, R. H. (2000). *Med. Phys.* **27**, 23–29.
ICRU (1989). International Commission on Radiation Units and Measurements Report No. 44. Bethesda: ICRU.
Joseph, P. M. & Spital, R. D. (1982). *Med. Phys.* **9**, 464–472.
Kieffer, J. (1938). *Am. J. Roentgenol.* **39**, 497–513.
Kyriakou, Y., Meyer, M. & Kalender, W. A. (2008). *Phys. Med. Biol.* **53**, N175–N185.
Lai, B., Khounsary, A. & Gluskin, E. (1993). Technical Bulletin ANL/APS/TB-11. Argonne National Laboratory/Advanced Photon Source, Argonne, IL, USA.
Lanczos, C. (1956). *Applied Analysis*. Princeton: Van Nostrand.
Levenberg, K. (1944). *Q. Appl. Math.* **2**, 164–168.
Limaye, A. (2006). *Drishti – Volume Exploration and Presentation Tool*. Poster presentation at the *2006 IEEE Visualization Conference*, Baltimore, MD, USA (see also http://anusf.anu.edu.au/Vizlab/drishti/index.shtml).
Lucy, L. B. (1974). *Astron. J.* **79**, 745–754.

research papers

McEwen, B. F., Downing, K. H. & Glaeser, R. M. (1995). *Ultramicroscopy*, **60**, 357–373.

McMaster, W. H., Del Grande, N. K., Mallett, J. H. & Hubbell, J. H. (1970). Report No. UCRL-50174. LLNL, Livermore, CA, USA.

McNitt-Gray, M. F. (2002). *Radiography*, **22**, 1541–1553.

Marquardt, D. W. (1963). *SIAM J. Appl. Math.* **11**, 431–441.

Matsushita, T. & Hashizume, H. (1983). In *Handbook on Synchrotron Radiation*, Vol. 1, edited by E. E. Koch, ch. 4. Amsterdam: North-Holland.

Matsushita, T. & Kaminaga, U. (1980). *J. Appl. Cryst.* **13**, 472–478.

Matsushita, T., Kaminaga, U. & Kohra, K. (1978). *Jpn. J. Appl. Phys.* **17**(Suppl. 2), 449–452.

Mayo, S. C., Davis, T. J., Gureyev, T. E., Miller, P. R., Paganin, D., Pogany, A., Stevenson, A. W. & Wilkins, S. W. (2003). *Opt. Express*, **11**, 2289–2302.

Merritt, R. B. & Chenery, S. G. (1986). *Phys. Med. Biol.* **31**, 55–63.

Meyer, M. (1998). PhD thesis, University of Lausanne, Switzerland.

Miller, M. K. (2000). *Atom Probe Tomography: Analysis at the Atomic Level.* New York: Kluwer Academic/Plenum.

Moffat, A. F. J. (1969). *Astron. Astrophys.* **3**, 455–461.

Morgan, K. S., Siu, K. K. W. & Paganin, D. M. (2010). *Opt. Express*, **18**, 9865–9878.

Naday, I., Ross, S., Kanyo, M., Westbrook, E. & Westbrook, M. (1994). *Nucl. Instrum. Methods Phys. Res. A*, **347**, 534–538.

Nakajima, N. (2007). *Phys. Rev. Lett.* **98**, 223901.

Natterer, F. (2001). *The Mathematics of Computerized Tomography.* Philadelphia: SIAM.

NBS (1976). Monograph 25, Section 13, p. 35. National Bureau of Standards, Washington, DC, USA.

Nuzzo, S., Peyrin, F., Cloetens, P., Baruchel, J. & Boivin, G. (2002). *Med. Phys.* **29**, 2672–2681.

Nyquist, H. (1928). *Trans. AIEE*, **47**, 617–644.

Ohnesorge, B., Flohr, T., Schwarz, K., Heiken, J. P. & Bae, K. T. (2000). *Med. Phys.* **27**, 39–46.

Orsi, T. H., Edwards, C. M. & Anderson, A. L. (1994). *J. Sediment. Res.* **64**, 690–693.

Paganin, D. M. (2006). *Coherent X-ray Optics, Oxford Series on Synchrotron Radiation*, No. 6. New York: Oxford University Press.

Paganin, D., Mayo, S. C., Gureyev, T. E., Miller, P. R. & Wilkins, S. W. (2002). *J. Microsc.* **206**, 33–40.

Pearson, K. (1916). *Philos. Trans. R. Soc. London Ser. A*, **216**, 429–457.

Pianetta, P. & Lindau, I. (1977). *J. Electron. Spectrosc. Relat. Phenom.* **11**, 13–38.

Pogany, A., Gao, D. & Wilkins, S. W. (1997). *Rev. Sci. Instrum.* **68**, 2774–2782.

Prager, P. R. (1971). PhD thesis, University of Melbourne, Australia.

Radon, J. H. (1917). *Ber. Verh. Königl. Sächs. Akad. Wiss. (Reports on the Proceedings of the Saxony Academy of Science)*, **69**, 262–277. [Translation by Parks, P. C. (1986). *IEEE Trans. Med. Imag.* **5**, 170–176.]

Rho, J. Y., Hobatho, M. C. & Ashman, R. B. (1995). *Med. Eng. Phys.* **17**, 347–355.

Richardson, W. H. (1972). *J. Opt. Soc. Am.* **62**, 55–59.

Roberto, J. B. & Batterman, B. W. (1970). *Phys. Rev. B*, **2**, 3220–3226.

Robertson, D. D., Weiss, P. J., Fishman, E. K., Magid, D. & Walker, P. S. (1988). *J. Comput. Assist. Tomogr.* **12**, 236–241.

Rustichelli, F., Romanzetti, S., Dubini, B., Girardin, E., Raven, C., Snigirev, A. & Rizzi, G. (2004). *J. Mater. Sci. Mater. Med.* **15**, 1053–1057.

Servidori, M., Cembali, F. & Milita, S. (2001). *Appl. Phys. A*, **73**, 75–82.

Shannon, C. E. (1949). *Proc. IRE*, **37**, 10–21.

Siewerdsen, J. H. & Jaffray, D. A. (2001). *Med. Phys.* **28**, 220–231.

Sijbers, J. & Postnov, A. (2004). *Phys. Med. Biol.* **49**, N247–N253.

Snigirev, A., Snigireva, I., Kohn, V., Kuznetsov, S. & Schelokov, I. (1995). *Rev. Sci. Instrum.* **66**, 5486–5492.

Spanne, P., Raven, C., Snigireva, I. & Snigirev, A. (1999). *Phys. Med. Biol.* **44**, 741–749.

Stevenson, A. W., Mayo, S. C., Häusermann, D., Maksimenko, A., Garrett, R. F., Hall, C. J., Wilkins, S. W., Lewis, R. A. & Myers, D. E. (2010). *J. Synchrotron Rad.* **17**, 75–80.

Tanaka, T. & Kitamura, H. (2001). *J. Synchrotron Rad.* **8**, 1221–1228.

Teague, M. R. (1983). *J. Opt. Soc. Am.* **73**, 1434–1441.

Tikhonov, A. N. & Arsenin, V. Y. (1977). *Solution of Ill-Posed Problems.* New York: Halsted.

Tran, C. Q., Barnea, Z., de Jonge, M. D., Dhal, B. B., Paterson, D., Cookson, D. J. & Chantler, C. T. (2003). *X-ray Spectrosc.* **32**, 69–74.

Trujillo, I., Aguerri, J. A. L., Cepa, J. & Gutiérrez, C. M. (2001). *Mon. Not. R. Astron. Soc.* **328**, 977–985.

Tsuchiyama, A., Uesugi, K., Nakano, T. & Ikeda, S. (2005). *Am. Mineral.* **90**, 132–142.

Vallebona, A. (1931). *Radiol. Med.* **17**, 1090–1097.

Vidal, F. P., Létang, J. M., Peix, G. & Cloetens, P. (2005). *Nucl. Instrum. Methods Phys. Res. B*, **234**, 333–348.

Wiener, N. (1949). *Extrapolation, Interpolation and Smoothing of Stationary Time Series.* New York: Wiley.

Wilkins, S. W., Gureyev, T. E., Gao, D., Pogany, A. & Stevenson, A. W. (1996). *Nature (London)*, **384**, 335–338.

Xu, S. & Li, R. (1988). *J. Appl. Cryst.* **21**, 213–217.

Yang, C.-K., Orphanoudakis, S. C. & Strohbehn, J. W. (1982). *Phys. Med. Biol.* **27**, 51–61.

Yang, Q. X., Xu, P. & Zheng, S. F. (2010a). *Sci. China Tech. Sci.* **53**, 512–518.

Yang, Y. S., Gureyev, T. E., Tulloh, A., Clennell, M. B. & Pervukhina, M. (2010b). *Meas. Sci. Tech.* **21**, 047001.

Young, R. A. & Wiles, D. B. (1982). *J. Appl. Cryst.* **15**, 430–438.

Zachariasen, W. H. (1945). *Theory of X-ray Diffraction in Crystals.* New York: Wiley.

Ziedses Des Plantes, B. G. (1932). *Acta Radiol.* **13**, 182–192.

Zschornack, G. (2007). *Handbook of X-ray Data.* Berlin: Springer.